Title
Evaluating Atmospheric River Impacts on Energy and Moisture Transport in the Arctic Using Different Detection Algorithms

Journal
Journal of Geophysical Research: Atmospheres, 131(4)

ISSN
2169-897X

Authors
Zhang, Chen
Cassano, John J
Seefeldt, Mark W
et al.

Publication Date
2026-02-28

DOI
10.1029/2025jd043335

JGR Atmospheres

RESEARCH ARTICLE
10.1029/2025JD043335

Special Collection:
The Arctic: An AGU Joint Special Collection

Evaluating Atmospheric River Impacts on Energy and Moisture Transport in the Arctic Using Different Detection Algorithms

Chen Zhang[1,2], John J. Cassano[1,2,3], Mark W. Seefeldt[1,2], Wen-wen Tung[4], Ankur Mahesh[5,6], and William D. Collins[5,6]

[1]Cooperative Institute for Research in Environmental Sciences, University of Colorado Boulder, Boulder, CO, USA, [2]National Snow and Ice Data Center, University of Colorado Boulder, Boulder, CO, USA, [3]Department of Atmospheric and Oceanic Sciences, University of Colorado Boulder, Boulder, CO, USA, [4]Department of Earth, Atmospheric, and Planetary Sciences, Purdue University, West Lafayette, IN, USA, [5]Lawrence Berkely National Laboratory, Berkely, CA, USA, [6]University of California, Berkele, Berkeley, CA, USA

Abstract Atmospheric rivers (ARs) significantly impact the Arctic climate system by enhancing atmospheric heat and moisture transport and altering the local energy budget. Developing AR detection tools (ARDTs) is critical yet challenging. This study evaluates 12 ARDTs in the Arctic to assess their performance in representing atmospheric heat (represented by moist static energy) and moisture transport, as well as surface downward longwave radiation (LWD) and precipitation impacts, spanning 2000 to 2019 using ERA5 reanalysis. We find that AR occurrence frequency in the Arctic varies widely, from less than 1% to over 13%, depending on the ARDT. This variability leads to differences in contributions to poleward atmospheric heat (<1%–33%) and moisture (<1%–49%) transport. The highest AR frequency, and corresponding contributions to atmospheric heat and moisture transport, occurs over the Atlantic sector during non-summer seasons for most ARDTs. This region aligns with the primary poleward moisture pathway and the end of climatological mid-latitude storm tracks, highlighting strong connections between Arctic ARs and mid-latitude cyclones. ARs induce significant LWD anomalies, largest in winter, smallest in summer, and also substantially contribute to the seasonal precipitation. Global ARDTs detect fewer ARs with larger anomalies (>100 W m^{-2} in higher Arctic), but contribute <1% to seasonal climatological LWD and precipitation. In contrast, polar-specific ARDTs detect higher AR occurrences and account for up to 16% of seasonal LWD and 41% precipitation. This suggests that algorithms emphasizing extreme events with large anomalies do not necessarily indicate a large climate radiative and precipitation impact.

Plain Language Summary Atmospheric rivers (ARs) are long narrow filaments of intense water vapor transport in the lower atmosphere that play a significant role in the Arctic climate. They bring heat and moisture into the region, influencing the energy balance and potentially accelerating sea ice loss and Arctic warming. However, detecting ARs in the Arctic is challenging because most AR detection tools (ARDTs) are designed for global or mid-latitudes, with few tailored for polar regions. This study evaluates 12 ARDTs to assess their ability to identify Arctic ARs and their contributions to heat, moisture transport, surface radiation, and precipitation impacts. Results show a wide range of AR detection frequencies, from less than 1% to over 13%, depending on the ARDT used. This variability significantly affects estimates of how much heat and moisture ARs transport into the Arctic. ARDTs designed/adapted for the Arctic detect more frequent ARs and show they contribute meaningfully to seasonal surface radiation and precipitation impacts. In contrast, global ARDTs, which focus on extreme moisture events in mid-latitudes, detect fewer ARs with larger radiation and precipitation anomalies but have reduced cumulative climate effects. These results emphasize the limitations of using global ARDTs in the Arctic context and should be avoided.

Key Points:

- AR detection tools (ARDTs) vary widely, leading to differences in Arctic AR frequency and heat and moisture transport impacts
- Polar ARDTs detect more ARs, contributing up to 33% heat, 49% moisture transport, 16% surface longwave radiation, and 41% precipitation
- Global ARDTs focus on extreme events with large anomalies but contribute as low as 1% to heat, moisture, radiative and precipitation impacts

Supporting Information:

Supporting Information may be found in the online version of this article.

Correspondence to:

C. Zhang and J. J. Cassano,
chen.zhang-3@colorado.edu;
john.cassano@colorado.edu

Citation:

Zhang, C., Cassano, J. J., Seefeldt, M. W., Tung, W.-w., Mahesh, A., & Collins, W. D. (2026). Evaluating atmospheric river impacts on energy and moisture transport in the Arctic using different detection algorithms. *Journal of Geophysical Research: Atmospheres*, *131*, e2025JD043335. https://doi.org/10.1029/2025JD043335

Received 8 JAN 2025
Accepted 21 JAN 2026

Author Contributions:

Conceptualization: Chen Zhang, John J. Cassano, Mark W. Seefeldt
Data curation: Chen Zhang, Wen-wen Tung

1. Introduction

Atmospheric rivers (ARs) are long and narrow filaments of enhanced moisture transport, typically associated with a low-level jet, in front of an extratropical cyclone (Ralph et al., 2018). ARs have been shown to be crucial in modulating the global hydrological cycle, accounting for more than 90% of total meridional moisture transport in the mid- and high-latitudes, despite occupying less than 10% of the Earth's circumference at any given latitude (Nash et al., 2018; Zhu & Newell, 1998). Although most literature focuses on the impacts of ARs on midlatitude

Formal analysis: Chen Zhang, John J. Cassano, Mark W. Seefeldt, Wen-wen Tung
Funding acquisition: Chen Zhang, John J. Cassano, Mark W. Seefeldt
Investigation: Chen Zhang, John J. Cassano, Mark W. Seefeldt
Methodology: Chen Zhang, John J. Cassano, Mark W. Seefeldt, Ankur Mahesh, William D. Collins
Project administration: John J. Cassano
Resources: John J. Cassano, Mark W. Seefeldt, Wen-wen Tung
Software: Wen-wen Tung
Supervision: John J. Cassano, Mark W. Seefeldt
Validation: Chen Zhang, John J. Cassano, Mark W. Seefeldt, Wen-wen Tung
Visualization: Chen Zhang, Mark W. Seefeldt
Writing – original draft: Chen Zhang
Writing – review & editing: Chen Zhang, John J. Cassano, Mark W. Seefeldt, Wen-wen Tung

precipitation (Chen et al., 2018; Lavers & Villarini, 2015; Luo & Tung, 2015; Neiman et al., 2008; Ralph et al., 2004, 2006; Leung & Qian, 2009, and others), ARs also penetrate polar regions and significantly affect the dry and cold environments (Gorodetskaya et al., 2014; Mattingly et al., 2018; Neff, 2018; Wille et al., 2019; C. Zhang et al., 2023; P. Zhang et al., 2023, and others).

ARs, and similar intense moisture intrusions, are recognized as key pathways for atmospheric moisture transport into and in the polar regions. Their contributions vary widely depending on the measurement methods, detection algorithms and specific regions: 28% of total poleward moisture transport across 70°N in the Arctic winter (Woods et al., 2013), 69% of total transient poleward moisture across 60°N in the Arctic winter and 66% in summer (Liu & Barnes, 2015), and more than 90% of total meridional moisture transport in high-latitude polar regions (Nash et al., 2018).

The Arctic's rapidly changing climate and Arctic amplification— the accelerated warming in the Arctic relative to the global average (e.g., Cohen et al., 2014; Graversen & Burtu, 2016; Graversen et al., 2008; Mortin et al., 2016; Serreze & Barry, 2011; Taylor et al., 2022)— have been increasingly linked to AR-related strong poleward moisture and heat flux transports. For instance, intense moisture intrusions, while constituting only 28% of the total poleward moisture transport, drive about 40% of the interannual variance in surface downward longwave radiation (LWD) and 30% in skin temperature in the Arctic during winter (Woods et al., 2013). Subsequent studies have shown that ARs and similar episodes of strong poleward moisture transport enhance atmospheric moisture and cloud cover in the Arctic, leading to increased LWD and surface warming. This results in reduced sea ice growth rate, including a record low in 2016–2017 (Hegyi & Taylor, 2018), and hinders sea ice recovery. The culmination of these impacts has resulted in a retreat of sea ice margins in recent decades (Woods & Caballero, 2016; P. Zhang et al., 2023). ARs also induce strong poleward sensible and latent heat transport, maintaining surface warming over the North Pacific during extended winters (Baggett et al., 2016). They also trigger Greenland ice sheet melt by inducing strong foehn effect and amplifying turbulent heat flux (Mattingly et al., 2018; Mattingly et al., 2020, 2023; Neff, 2018). A recent comprehensive study highlights the significant seasonal and land-sea-sea ice contrasts in AR-induced surface energy budgets (SEB) impacts of the Arctic as a result of ARs (C. Zhang et al., 2025).

In Antarctica, ARs have multifaceted impacts on the surface mass balance. They cause strong localized snowfall accumulation in East Antarctica (Gorodetskaya et al., 2014). They also play a role in surface melting events over the West Antarctic ice sheet due to strong integrated water vapor (IWV) and cloud-radiative effects, warming the surface through increased LWD and sensible heat flux as well as reduced surface albedo via rainfall (Wille et al., 2019). Studies using a particularly restrictive AR detection and tracking method found that ARs occurring during only 1%–3% of the year contribute to 40% of extreme precipitation (Wille et al., 2021) and 11% of the annual surface accumulation (Maclennan et al., 2023).

Developing AR detection and tracking methods is critical yet challenging. The Atmospheric River Intercomparison Project (ARTMIP) has spurred the development of numerous AR detection and tracking methods, each with different detection criteria tailored to specific purposes (Collow et al., 2022b; O'Brien et al., 2020, 2022; Rutz et al., 2019; Shields et al., 2018). Many AR detection tools (ARDTs) within ARTMIP are designed for mid-latitudes and focus on extreme events. Examples include the satellite-based method using IWV content greater than 20 mm (Ralph et al., 2004, 2006), the reanalysis-based absolute integrated water vapor transport (IVT) threshold of $\geq$250 kg $m^{-1}s^{-1}$ (Rutz et al., 2014), and the percentile-based IVT threshold (e.g., the 85th percentile of climatological thresholds) (Lavers et al., 2012; Lavers & Villarini, 2013). Additional ARDTs have been developed, drawing on similar AR detection approaches inspired by these seminal methods.

More recently, some ARDTs have been specifically tailored for use in polar regions. e.g., Gorodetskaya et al. (2014) developed a new IWV threshold to detect ARs in Antarctica by considering the decreased saturation capacity of the polar troposphere (i.e., a temperature-adjusted criteria). This newly defined IWV threshold meets the 20 mm IWV value at lower latitudes of 40°–50°S but drops to slightly below 10 mm near the Antarctic coast, effectively capturing strong precipitation events in East Antarctica. To ensure consistency with the AR detection results in East Antarctica by Gorodetskaya et al. (2014), Guan and Waliser (2015) applied an additional 100 kg m^{-1} s^{-1} to supplement the seasonal 85th percentile climate thresholds of IVT in the polar regions during their global AR detection work. Similarly, Wille et al. (2019, 2021) applies a monthly 98th percentile climate threshold on IVT, IWV, or poleward IVT to be consistent with the results in Gorodetskaya et al. (2014). Other

similar or adapted ARDTs have been developed in various polar AR studies (Ma et al., 2021, 2024; Mattingly et al., 2018; C. Zhang et al., 2023).

The selection of an AR detection method can significantly affect the identified characteristics of ARs, and consequently, the associated impacts (Shields et al., 2018). For example, in mid-latitudes, AR frequency, duration, and seasonality exhibits a wide range of results based on different ARTMIP methods (Rutz et al., 2019). In the polar regions, Antarctic-specific ARDTs developed by Wille et al. (2021) tend to identify more ARs inland over the ice sheets, compared to most global ARDTs (Shields et al., 2022). In the Arctic, restrictive AR detection criteria emphasize impacts for individual cases but minimize AR contributions to the overall climatology of the SEB due to their low occurrence frequency (C. Zhang et al., 2025). Moreover, studies have found that the uncertainty arising from different AR detection methods is significantly greater than the uncertainty from model or reanalysis differences (Collow et al., 2022b; O'Brien et al., 2022; Shields et al., 2022).

While efforts to systematically compare different ARDTs are ongoing (e.g., O'Brien et al., 2022; Rutz et al., 2019; Shields et al., 2018, 2022), the relationships between ARs and the moisture or energy budgets of the Arctic across a variety of AR indices remain to be quantified. Most existing intercomparison studies focus on mid-latitudes or Antarctica, and little is known about how different ARDTs perform in the unique thermodynamic and dynamic environment of the Arctic. As ARs are increasingly recognized as key drivers of the Arctic amplification, a wide range of ARDTs have been applied in Arctic studies, yet their relative performance in this region remains unclear. This study is the first to comprehensively evaluate and compare the performance of 12 widely used polar and global ARDTs in detecting ARs and quantifying their impacts on atmospheric heat and moisture transport, LWD and precipitation across the entire Arctic domain (north of 60°N). By doing so, it not only reveals methodological differences in AR detection but also highlights their implications for understanding Arctic climate processes.

This work establishes a unified intercomparison framework to analyze AR-driven atmospheric energy and moisture transport and associated surface impacts and to address three key questions. These key questions include: (a) The extent to which ARs contribute to atmospheric heat and moisture transport in the Arctic, and how this varies spatially; (b) The impacts of ARs on LWD and total precipitation, and their climatological contribution to Arctic LWD and total precipitation; and (c) How the above-mentioned impacts vary across different ARDTs. The paper is structured as follows: Section 2 describes the data and methods. Sections 3–5 analyze and discuss AR occurrence frequency, atmospheric heat and moisture transport, and consequent LWD and total precipitation impacts associated with different ARDTs, respectively. Section 6 provides discussion and conclusions.

2. Data and Methods

2.1. AR Detection Algorithms

A total of 12 ARDTs that cover the Arctic region (60°N north) are used for this intercomparison (Table 1). Six of them were contributed directly by the developers of the ARDTs, and six were retrieved from the ARTMIP Tier 2 Catalogs (Collow et al., 2022b) using the fifth generation of ECMWF atmospheric reanalysis (ERA5, Hersbach et al., 2020). In ARTMIP Tier 2, each participating ARDT submitted their binary tags for AR detection with a temporal resolution of 1 hr and a spatial resolution of 0.25° × 0.25°, covering either 20 years from 2000 to 2019 or 41 years from 1979 to 2019. For the other six ARDTs, the temporal resolutions range from 3 hourly to 6 hourly, and spatial resolutions are 0.25° × 0.25° or 1° × 1°. We focus on AR indices in ERA5 because it is considered a state-of-the-art global reanalysis for the Arctic (Graham et al., 2019). Additionally, it has been found that between the two common reanalyzes used in AR research, the 0.25° × 0.25° ERA5 IVT field is more precise than the coarser-resolution 0.5° × 0.625° MERRA-2 (NASA Modern-Era Retrospective Analysis for Research and Applications, version 2, Gelaro et al., 2017) IVT for AR detection and tracking (C. Zhang et al., 2023). A brief summary of the 12 ARDTs is listed in Table 1. It is important to note that three ARDTs have AR detection domains that do not encompass the entire Arctic region (from 60°N to 90°N). Specifically, the spatial AR detection domains for Wille-vIVT and Wille-IWV are limited to regions at or below 85°N, while TempestLR is restricted to areas at or below 79°N. Therefore, in the subsequent analysis, we visualize the results within these specific AR detection domains when presenting the findings based on these three ARDTs, while for other ARDTs, the entire Arctic region is considered.

Table 1
List of the 12 AR Detection Algorithms Included in the Intercomparison

		ARTMIP Tier 2	Climate percentile	Threshold (kg m^{-1} s^{-1})	Length (km)	Length: Width	Duration (hours)	Spatial coverage	Spatial resolution	Temporal resolution	Reference
Polar-Specific	Purdue-85th IVT	N	85th IVT	-	≥1,500	≥2	18	≥35°N	0.25° × 0.25°	3-hourly	C. Zhang et al. (2023)
	Guan-Waliser	Y	85th IVT	100	>2,000	>2	–	global	0.25° × 0.25°	1-hourly	Guan and Waliser (2015)
	Mattingly[b]	N	85th IVT	150	>1,500	>1.5	–	≥10°N	0.25° × 0.25°	3-hourly	Mattingly et al. (2018)
	M24[c]	N	85th IVT	100	>1,500	>2	–	global	1.0° × 1.0°	6-hourly	Ma et al. (2024)
	Gorodetskaya[d]	N	–	Temp. Adjusted saturated IWV	>2,000	<40° longitude	–	global	0.25° × 0.25°	1-hourly	Lauer et al. (2023)
	Wille-vIVT[e]	N	98th vIVT	–	>2,000	–	–	37.5°N to 85°N	1.0° × 1.0°	3-hourly	Wille et al. (2021)
	Wille-IWV[e]	N	98th IWV	–	>2,000	–	–	37.5°N to 85°N	1.0° × 1.0°	3-hourly	Wille et al. (2021)
Global	Mundhenk v3[f]	Y	–	Anomalous 250	≥1,400	≥1.6	–	global	0.25° × 0.25°	1-hourly	Mundhenk et al. (2016)
	Lora v2[g]	Y	–	225 & Latitudinally dependent	>2,000	–	–	global	0.25° × 0.25°	1-hourly	Skinner et al. (2020)
	AR-Connect[h]	Y	–	700/300	–	–	24	≥23.5°N	0.25° × 0.25°	1-hourly	Shearer et al. (2020)
	TempestLR[i]	Y	See notes		area ≥1.25 × 10^5 km		–	15°N to 79°N	0.25° × 0.25°	1-hourly	McClenny et al. (2020)
DL	ClimateNet[j]	Y	See notes		–	–	–	global	0.25° × 0.25°	1-hourly	Prabhat et al. (2021)

[a]Coherence in IVT directions with a poleward mean IVT direction; consistency between object mean IVT direction and overall orientation. [b]AR must penetrate 66.56°N; zonal wind >2 m s^{-1} if object centroid <35°N; meridional wind >0 if object centroid <66.56°N. [c]Based on Guan and Waliser (2019) with slight modifications to criteria; coherence in IVT directions with a poleward mean IVT direction. [d]Based on Gorodetskaya et al. (2020, 2014), IWV ≥ zonal mean plus a temperature adjusted saturated IWV, with the object has to reach and cross 70°N. [e]The meridional segments extend at least 20° in the meridional direction (~length >2,000 km). [f]Threshold is for IVT anomal by removing IVT climatological mean and seasonality. [g]A latitudinally and temporally dependent relative IVT threshold that requires zonal mean IWV values. [h]Threshold of IVT is ≥700 kg m^{-1} s^{-1} for AR core and ≥300 kg m^{-1} s^{-1} for AR boundary. [i]The Laplacian of IVT is < −40,000 kg m^{-1} s^{-1} rad^{-2} (meets IVT >250 kg m^{-1} s^{-1}). [j]Deep learning-based segmentation; trained on 500 expert labeled images of various variables, including IVT, IWV, vorticity, surface wind vectors, 850 hPa wind vectors, and sea level pressure.

The 12 ARDTs used in this study (Table 1) apply a variety of methods to detect ARs, including climate-percentile and absolute thresholds on IVT or IWV, as well as AR geometry and/or temporal criteria. Some of the algorithms are global, including the Arctic region, while others are specifically designed for Arctic or polar regions, or are global with polar adjustments. Here we focus on the most recent 20 years from 2000 to 2019 to incorporate as many ARDTs as possible and to facilitate intercomparison among the same common periods. Additionally, C. Zhang et al. (2021) found that climate criteria and moisture fields significantly affect the utility of the generated AR index for describing AR-related surface hydrometeorological impacts. Therefore, according to the AR climate thresholds and the application of ARs in polar or global regions, we divide the 12 ARDTs into three categories.

The first category includes seven *polar-specific* ARDTs. This group includes the Purdue-85th-IVT ARDT, which is Arctic-specific, and applies monthly 85th percentile climate thresholds on the IVT detection values without additional absolute constraints. The three other *polar-specific* ARDTs include M24, Guan-Waliser, and Mattingly ARDTs, which apply an additional absolute threshold of 100 or 150 kg m^{-1} s^{-1} to supplement the 85th percentile climate thresholds and here are considered as *polar-constrained* ARDTs. According to Guan and Waliser (2015), the lower limit of 100 kg m^{-1} s^{-1} was selected to isolate AR-like features in the polar regions and to be consistent with the AR detection results associated with the extreme precipitation events in East Antarctica by Gorodetskaya et al. (2014). Moreover, Gorodetskaya AR detection algorithm (Gorodetskaya et al., 2014, 2020; Lauer

et al., 2023) identifies ARs by applying thersholds to IWV based on the contrast between zonal mean and maximum staturated IWV, accouting for polar saturation limits with a scaling coefficient. Furthermore, the Wille-vIVT- and Wille-IWV-based ARDTs (Wille et al., 2019, 2021) are two additional *polar-specific* ARDTs that here are considered as *polar-extreme* ARDTs. These two ARDTs apply a more restrictive 98th percentile climate threshold on poleward IVT or IWV. By using these more restrictive climate thresholds, they detect 90% of the ARs identified by Gorodetskaya et al. (2014).

The second category includes four *global-specific* ARDTs—the Mundhenk_v3, Lora_v2, AR-Connect, and TempestLR. These ARDTs utilize a range of restrictive relative and absolute thresholds of IVT, or the Laplacian of IVT, to satisfy IVT thresholds exceeding at least 225–700 kg m^{-1} s^{-1} (see Table 1 for ARDT details). The common absolute IVT threshold of 250 kg m^{-1} s^{-1} was initially developed to better correspond to the spatial extent of heavy precipitation over the West Coast of North America (Rutz et al., 2014). Therefore, this second category of ARDTs primarily focuses on detecting ARs in the mid-latitudes. The third category is *deep learning*-based ARDTs (DL ARDT), and includes one ARDT, ClimateNet. Similar to the second category of *global-specific* ARDTs, ClimateNet ARDT is designed to detect ARs in the mid-latitudes.

2.2. Heat and Moisture Transport, Surface Downward Longwave Radiation and Surface Total Precipitation in ERA5

Reanalysis data are crucial for the Arctic due to the sparse in situ observations in this region. In this study, we use the ERA5 reanalysis, released by the ECMWF in 2019, which is the latest reanalysis product, offering high spatial ($0.25° \times 0.25°$) and temporal (hourly) resolutions. ERA5 is based on the ECMWF Integrated Forecasting System (IFS) CY41r2, utilizing 4D-Var data assimilation and model forecasts with 137 hybrid sigma/model levels up to 1 hPa in the vertical (Hersbach et al., 2020).

Moist static energy (MSE, defined as Equation 1), including sensible heat, latent heat, and potential energy, encompasses all relevant forms of energy involved in atmospheric processes because kinetic energy is typically a small component of the energy budget and can be ignored (Serreze et al., 2007). Therefore, MSE transport is crucial for understanding and computing atmospheric energy and heat transport.

$$\mathrm{MSE} = C_p \cdot T + \varnothing + L_v \cdot q \tag{1}$$

Where $C_p = 1005$ J $(\mathrm{kg} \cdot \mathrm{K})^{-1}$ is the specific heat at constant pressure, T is the atmospheric temperature (in K), $\varnothing$ is the geopotential (in m^2 s^{-2}), $L_v = 2.5 \times 10^6$ J kg^{-1} is the latent heat of vapourization and q is the specific humidity (in kg kg^{-1}).

Because reanalysis data does not conserve mass, the calculation of MSE transport requires a mass correction (Clark et al., 2022; Cox et al., 2023, 2024; Mahesh et al., 2025). Following their approach, the mass corrected total MSE transport and IVT at a given latitude can be computed as follows,

$$\text{Instantaneous MSE transport } (\theta) = \frac{2\pi a \cos(\theta)}{g} \int_{P_T}^{\overline{P_s}} \left([\mathrm{MSE}]^+ [v]^+ + [\mathrm{MSE}^* v^*] \right) dp \tag{2}$$

$$\text{Instantaneous IVT } (\theta) = \frac{2\pi a \cos(\theta)}{g} \int_{P_T}^{\overline{P_s}} \left([q]^+ [v]^+ + [q^* v^*] \right) dp \tag{3}$$

where θ is the latitude, a is the Earth's radius, $\overline{P_s}$ is the time-mean surface pressure (in Pa), $P_T = 1$ hPa denotes the top of atmospheric vertical levels in ERA5, v is the meridional wind component (in m s^{-1}) and p is pressure (in Pa). The brackets [·] denote a zonal mean, asterisks (*) are departures from the zonal average, and swords (+) are departures from the vertical average. The detailed mass-correction procedure is described in Cox et al. (2023, 2024) and Equation 2 above is identical to Equation 2 in Cox et al. (2024).

For the analysis presented below we need to resolve the heat and moisture transport at each ERA5 grid point at each instantaneous time step. This requires that we do not apply the zonal average used by Cox et al. (2024). The grid point MSE transport can be calculated as:

$$\text{MSE transport}_{\text{grid}} = \frac{1}{g}\int_{P_T}^{\overline{P_s}} \left([\text{MSE}]^+[v]^+ + [v]\,\text{MSE}^* + [\text{MSE}]\,v^* + \text{MSE}^* v^*\right) dp \quad (4)$$

This equation contains two additional terms compared to Equation 2, $[v]\,\text{MSE}^*$ and $[\text{MSE}]\,v^*$, which go to zero when a zonal average is applied as in Cox et al. (2024) but are non-zero when considering individual grid points.

As in Cox et al. (2023, 2024), the zonal-mean meridional wind is further decomposed into a vertical mean and deviations from that vertical mean, $[v] = \widehat{[v]} + [v]^+$, where $\widehat{[v]}$ is assumed to be zero under the constraint of no net mass transport across a latitude circle. With this assumption, the grid-point meridional MSE transport, explicitly referenced to the zonal-mean state, can be expressed as:

$$\text{MSE transport}_{\text{grid}} = \frac{1}{g}\int_{P_T}^{\overline{P_s}} \left([\text{MSE}]^+[v]^+ + [v]^+\text{MSE}^* + [\text{MSE}]\,v^* + \text{MSE}^* v^*\right) dp \quad (5)$$

Using the same zonal-mean-based decomposition, the grid-point meridional integrated vapor transport (IVT) at each instantaneous time step is calculated as:

$$\text{IVT}_{\text{grid}} = \frac{1}{g}\int_{P_T}^{\overline{P_s}} \left([q]^+[v]^+ + [v]^+ q^* + [q]\,v^* + q^* v^*\right) dp \quad (6)$$

It is noted that latent heat transport in Equation 5 corresponds to the latent heat of vaporization, L_v, multiplied by IVT in Equation 6. We are particularly interested in evaluating the impacts of ARs on poleward MSE transport and poleward IVT in the Arctic, specifically when the calculated MSE transports in Equation 5 and IVT in Equation 6 are directed poleward (positive).

Additionally, we retrieved hourly LWD (in J m^{-2}) and hourly accumulated surface precipitation (in m) from ERA5. To be consistent with the AR index's hourly data and to quantify AR-related LWD and precipitation over the Arctic, accumulated surface LWD fluxes (J m^{-2}) and surface precipitation (m) are converted to hourly mean surface fluxes (W m^{-2}) and hourly precipitation rate (m hr^{-1}), considered as instantaneous values at the center of each hour (e.g., 00:30, 01:30 UTC). These values are then linearly interpolated to the start of each hourly period (e.g., 00 UTC, 01 UTC).

As mentioned above, the temporal resolutions across the 12 ARDTs range from 1 hr, 3 to 6 hr, with most *polar-specific* ARDTs being 3-hourly, and *global-specific* and DL ARDTs being 1-hourly. To facilitate better intercomparison of AR-related MSE transport, IVT, LWD, and surface precipitation impacts in the Arctic based on these 12 ARDTs, we downsample the 1-hourly ARDTs (i.e., Gorodetskaya ARDT, Guan-Waliser ARDT, *global-specific* and DL ARDTs) to 3-hourly intervals, while maintaining the 6-hourly resolution for M24 ARDT. Accordingly, we downsample the time series of MSE, IVT, LWD and total precipitation to 3-hourly intervals (or 6-hourly for the M24 ARDT) to align with the temporal resolution of the ARDTs. Similarly, we retain the original 0.25° × 0.25° ERA5 spatial resolution of ARDTs and corresponding variables, while downsampling them to a 1° × 1° spatial resolution for the M24, Wille-vIVT and Wille-IWV ARDTs during the intercomparisons.

3. Variability of AR Occurrence Frequency Due To ARDTs

The latitudinal change of zonal mean AR occurrence frequency in the Arctic, from 60°N to 88°N, identified by 12 ARDTs during each season over 2000–2019, are shown in Figure 1a. Overall, Figure 1a demonstrates a significant decrease in identified ARs as the climate criteria, or thresholds, increase across the ARDTs. Specifically, AR occurrence frequency is highest with *polar-specific* ARDTs using the 85th percentile climate thresholds. However, incorporating the additional absolute IVT thresholds of 100 or 150 kg m^{-1} s^{-1} results in lower AR frequencies for *polar-constrained* ARDTs (i.e., Guan-Waliser, M24, and Mattingly ARDTs), compared to Purdue-85th-IVT ARDT. Quantitively, the identified AR occurrence frequency ranges from 10.4% to 13.6% for Purdue-85th-IVT ARDT to 0.4%–11% for polar-constrained ARDTs, between the latitudes 60°N and 80°N. Their differences are most pronounced in winter and spring, but minimal in summer, largely due to the fact that the 85th percentile climate threshold falls below 100 kg m^{-1} s^{-1} in most of the Arctic domain in cold seasons (especially in

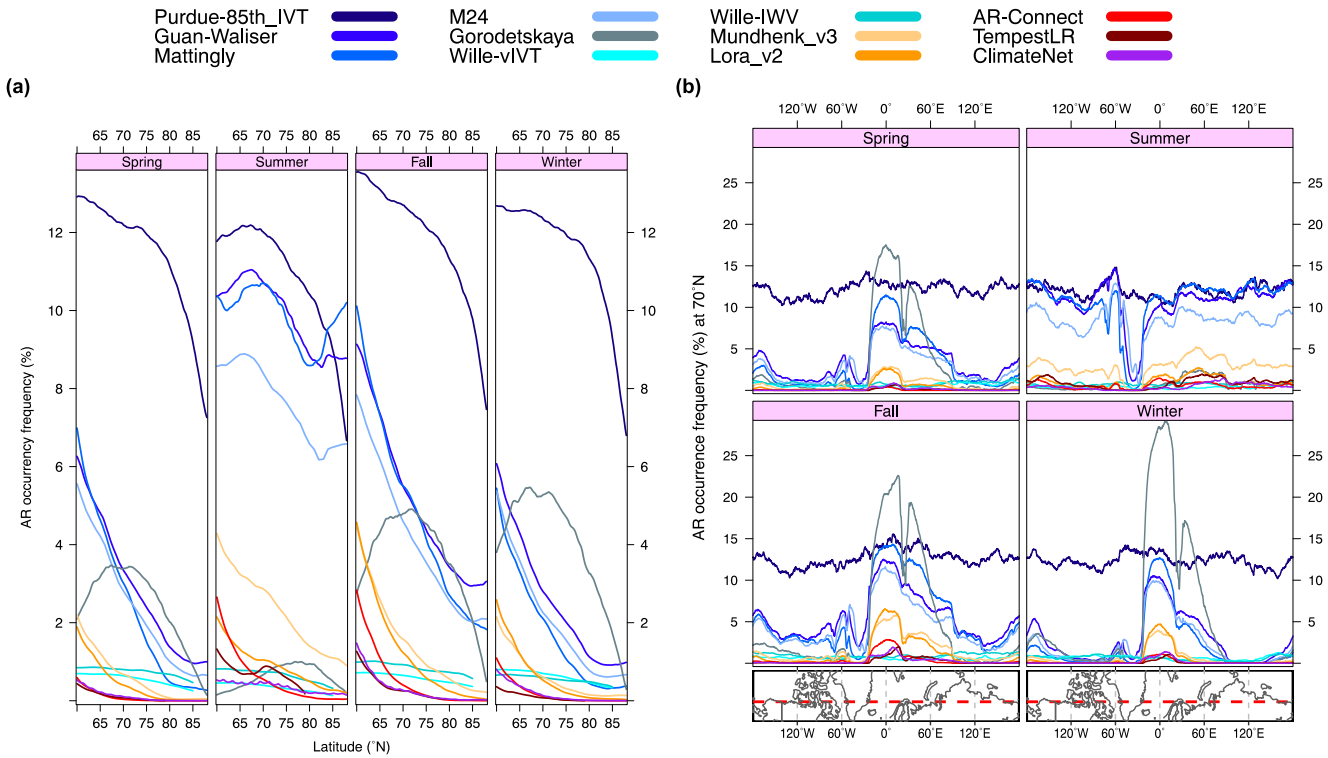

Figure 1. (a) Zonal mean distribution of AR occurrence frequency (unit: %) as a function of latitude from 60°N to 88°N during each season (Spring: Mar–May, Summer: Jun–Aug, Fall: Sep–Nov, Winter: Dec–Feb) from 2000 to 2019 using 12 ARDTs. (b) Longitudinal distribution of AR occurrence frequency (unit: %) at 70°N during each season detected by all 12 ARDTs. An Arctic map showing the region crossing the 70°N (red dotted line) is displayed at the base of each panel.

winter) (C. Zhang et al., 2023, 2025). The Gorodetskaya ARDT detects AR frequency ranging from 2% to 5.5% during non-summer seasons, aligning with the range of *polar-constrained* ARDTs with the absolute thresholds. In summer, however, its detected frequencies largely drop to a range of 0.15%–1% between 60°N and 80°N, comparable to those using non-polar ARDTs. Other ARDTs exhibit considerably lower AR occurrence frequencies, ranging from 0.0% to 4.6% between 60°N and 80°N, due to the more restrictive thresholds applied. Specifically, within these ARDTs, detected AR occurrences decrease with increasingly restrictive climate thresholds, from Mundhenk_v3 (using absolute thresholds of IVT anomaly ≥250 kg m^{-1} s^{-1}) and Lora_v2 (using both absolute of 225 kg m^{-1} s^{-1} and relative thresholds depending on the zonal mean IWV), across AR-Connect (using absolute thresholds of 700 kg m^{-1} s^{-1}) and *polar-extremes* ARDTs (using 98th percentile climate thresholds) to TempestLR (using Laplacian of IVT < −40,000 kg $m^{-1}s^{-1}rad^{-2}$) and DL ARDTs. The DL-based ClimateNet ARDT is trained to detect strong AR features in the midlatitudes and may underperform in the Arctic where AR signals are weaker and less distinct.

From 60°N to higher latitudes, absolute threshold-based ARDTs (*polar-constrained* and *global-specific*) and the DL ARDT detect ARs decreasing dramatically, and beyond 80°N the magnitudes decrease to ~0% for *global-specific* and DL ARDTs, and less than 1% for *polar-constrained* ARDTs in winter, spring and fall. The DL ARDT tends to capture extreme AR signals in the midlatidues and behaves similarly to global-specific ARDTs that are designed to identify intense precipitation. The percentile-based ARDTs (Purdue-85th_IVT and *polar-extreme* ARDTs) exhibit smaller meridional variability due to their grid-point-dependent climate thresholds, with AR frequency dropping off only at the highest latitudes for Purdue-85th_IVT. In summer, the 85th-percentile climate threshold exceeds the absolute threshold used in the *polar-constrained* ARDTs resulting in only a gradual decrease of AR occurrence frequency for all *polar-specific* ARDTs in this season. The Purdue-85th-IVT and *polar-extreme* ARDTs display little seasonality, compared to other ARDTs. The lack of strong latitudinal variability and seasonality could be attributable to their percentile-only based, grid point- and monthly (seasonal)- dependent climate threshold detection algorithms. While the *polar-constrained* ARDTs with an absolute threshold of 100 or 150 kg m^{-1} s^{-1} exhibit much stronger seasonality in the Arctic, AR frequencies are

much larger in the summer season compared to spring, fall and winter. Interestingly, the Gorodetskaya ARDT displays the opposite seasonality, with maximum AR occurrence between 65°N and 75°N during non-summer seasons. This distinct pattern likely arises from its detection algorithm, which uses a relative threshold based on saturated IWV and requires ARs to reach and cross 70°N, making it more sensitive to cold-season moisture anomalies and less likely to detect ARs in summer when saturated IWV is higher. North of 70°N, its AR occurrence pattern closely resembles thsother *polar-constrained* ARDTs with absolute thrresholds, particularly in fall and spring, and to a lesser extent in winter. In summer, however, the Gorodetskaya ARDT identifies far fewer ARs, with the magnitudes similar to those identified by the *Polar-extreme* ARDTs, and a maximum occurrence near 80°N.*Global-specific* and DL- ARDTs display a weaker seasonality in the Arctic due to the smaller frequency of ARs with slightly more ARs in fall and summer, less in winter and a minimum in spring. Overall, the absolute threshold-based ARDTs using more restrictive criteria tend to detect only the most extreme AR events.

Figure 1b visualizes the longitudinal distribution of seasonal mean AR occurrence frequency identified by the 12 ARDTs at 70°N. Due to the nature of percentile-based climate thresholds for each grid point at each month, Purdue-85th-IVT ARDT and *polar extreme* ARDTs show little longitudinal variability, compared to the other ADRTs. In non-summer seasons (winter, spring and fall), the other ARDTs indicate that ARs occur more frequently over oceans than over land. The highest AR occurrence frequency is observed in the Arctic Atlantic sector extending to the Barents-Kara Seas, with the maximum ranging from 29% for Gorodetskaya ARDT, 11.6%–15.5% for *polar-specific* ARDTs using the 85th percentile climate thresholds, to 2%–6.6% for *global-specific* and DL ARDTs. The particularly high AR frequency detected by the Gorodetskaya ARDT is likely due to its use of temperature-adjusted saturated IWV and its criterion that ARs must corss 70°N. The next highest AR occurrences are over the Arctic Pacific sector and Baffin Bay. These highest AR occurrences over the Arctic Atlantic and Pacific sectors correspond to the climatologically stronger IVT or IWV regions, where the ends of the two extratropical storm tracks are located. In summer, consistent with the climatological minima of IWV or IVT over Greenland, the detected AR occurrence frequency is lowest over central Greenland for most ARDTs (with a minimum AR frequency ranging from 0.2% for *polar-constrained* ARDTs to ∼0% for *global-specific* and DL ARDTs), except for the Purdue-85th-IVT ARDT, which shows a higher frequency (∼11%) due to its percentile-, grid point-based detection algorithm.

4. Role of ARs in Atmospheric Heat and Moisture Transport

ARs are well-known for their ability to transport large amounts of heat and moisture poleward from mid-latitudes, significantly influencing the Arctic environment. Assessing AR-related heat and energy budgets has been recognized as an important area of research within the AR community (Ralph et al., 2017). In the Arctic, understanding these budgets is particularly crucial due to their potential impacts on sea ice extent, surface warming, and the melting of the Greenland ice sheet (e.g., Hegyi & Taylor, 2018; Mattingly et al., 2018; P. Zhang et al., 2023). In this study, we aim to quantify the extent to which meridional heat and moisture transport, specifically the portion that carries heat and moisture poleward to the Arctic region, can be attributable to ARs. We calculate the ratio of AR-related poleward MSE transport (i.e., the MSE transport within the detected ARs, referred to AR_MSET$_P$), to the total poleward MSE transport (MSET$_P$) for each ARDT. This ratio indicates the fraction of all poleward MSE transport attributable to ARs. Additionally, we compare the magnitude of AR contributions to poleward MSE transport relative to how often the ARs occur, expressed as the ratio of AR-MSE contribution to corresponding AR frequency ($\frac{\text{AR\_MSE contribution}}{\text{AR frequency}}$). Similarly, we assess AR contributions to poleward moisture transport using the same approach with IVT instead of MSE transport.

4.1. AR Contributions to Atmospheric Heat Transport

Figures 2a and 2c illustrate the zonal ratio of AR_MSET$_P$ to MSET$_P$ ($\frac{\text{AR\_MSET}_P}{\text{MSET}_P}$), which is the fractional AR contribution to poleward MSE transport, as a function of latitude from 60°N to 88°N, and the longitudinal distribution of $\frac{\text{AR\_MSET}_P}{\text{MSET}_P}$ at 70°N, respectively, derived from each ARDT during each season. Figure 2b illustrates the comparison of the zonal AR contribution to poleward MSE transport (Figure 2a) with their corresponding frequency (Figure 1a) from 60°N to 88°N, expressed as the ratio $\frac{\text{AR\_MSE contribution}}{\text{AR frequency}}$. The corresponding zonal and longitudinal distribution for MSET$_P$ and AR_MSET$_P$ for each ARDT are provided in Figure S1 of Supporting Information S1. Similarly, Figure S2 in Supporting Information S1 shows the corresponding figures for total

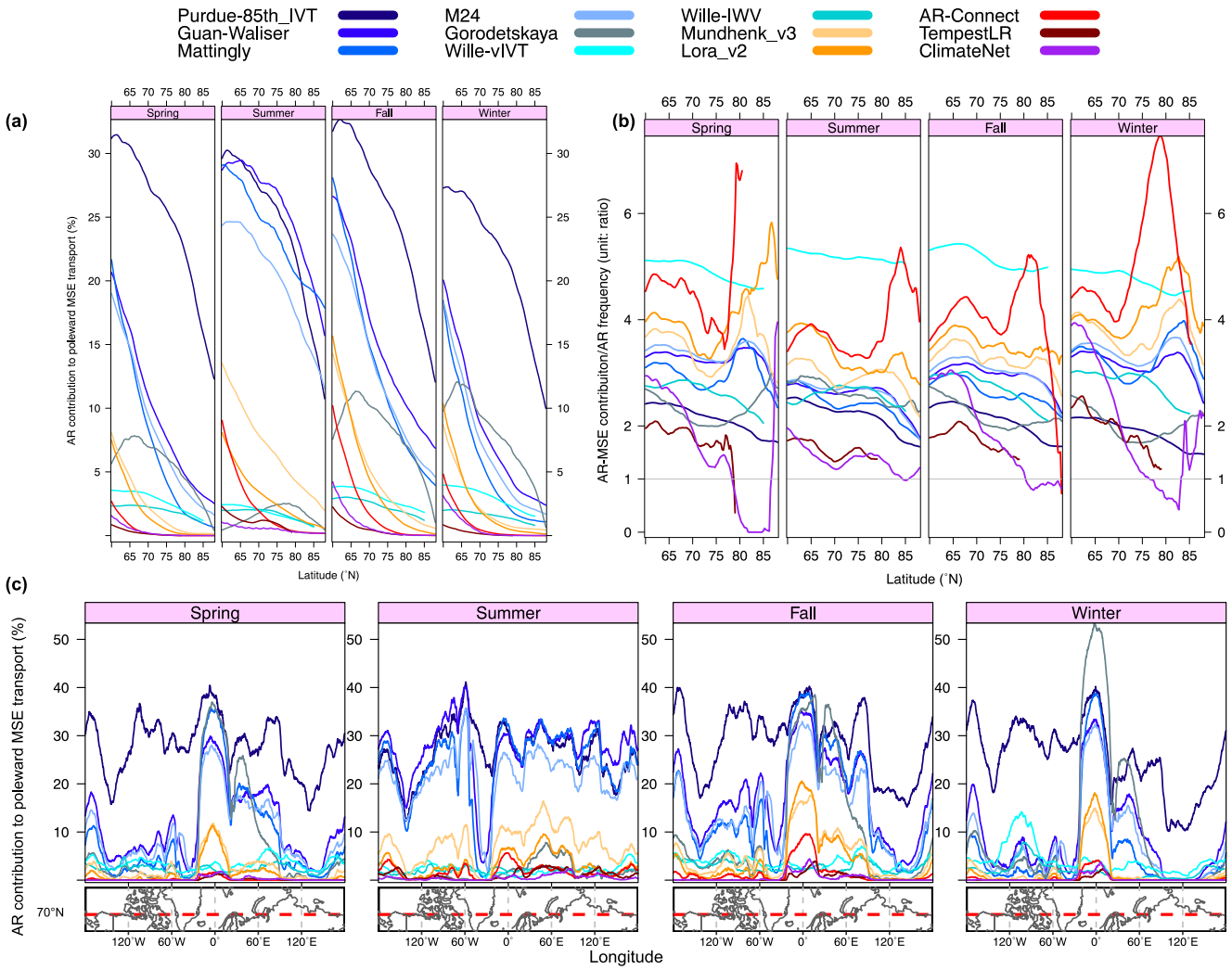

Figure 2. (a) Zonal distribution of AR contribution to total poleward MSE transport ($\frac{AR\_MSET_P}{MSET_P}$, unit: %) at each latitude from 60°N to 88°N during each season (Spring: Mar–May, Summer: Jun–Aug, Fall: Sep–Nov, Winter: Dec–Feb) from 2000 to 2019 using 12 ARDTs. (b) Zonal distribution of the ratio of AR contribution to total poleward MSE transport (panel (a)) to AR occurrence frequency (Figure 1a) from 60°N to 88°N during each season. (c) Longitudinal distribution of AR contribution to total poleward MSE transport ($\frac{AR\_MSET_P}{MSET_P}$, unit: %) at 70°N during each season detected by all 12 ARDTs. An Arctic map showing the region crossing the 70°N (red dotted line) is displayed at the base of each panel.

meridional (both poleward and equatorward) MSE transport and AR-related total meridional MSE transport, for each ARDT during each season.

As shown in Figure 2a, there is a wide range of AR contributions to poleward MSE transport, resulting from the varying AR occurrence frequencies depicted in Figure 1a. The extent to which ARs contribute to poleward MSE transport is strongly influenced by their occurrence frequency, as a result of different AR detection criteria. Less restrictive detection criteria, such as the Purdue-85th-IVT ARDT, account for the largest total poleward MSE transport, ranging from 10% to 33% (Figure 2a), which is 1.5–2.5 times the corresponding AR occurrence frequency (Figure 2b). When additional absolute thresholds of 100 or 150 kg m^{-1} s^{-1} are applied, *polar-constrained* ARDTs contribute smaller percentages to poleward MSE transport, ranging from 1% to 29%, which is 1.7–4 times their corresponding AR occurrence frequency. Consistent to Figure 1a, the Gorodetskaya ARDT shows maximum MSE transport between 65°N and 70°N during non-summer seasons. North of 70°N, its pattern resemble that of *Polar-constrained ARDT*, with contributions ranging from 0.4% to 12%, around 1.7 to 3 times of its frequency. In summer, when fewer ARs are detected, the associated MSE transport is also slower, ranging from 0.4% to 2.5%, 2.3–3 times the frequency. *Global-specific* and DL ARDTs, which use more restrictive detection

criteria, result in lower contributions of ARs to poleward MSE transport. Specifically, ARDTs such as Mundhenk_v3, Lora_v2, and AR-Connect correspond to 0%–16% of poleward MSE transport, while AR contributions using TempestLR and DL ARDTs are about 0%–4%. Despite their smaller total contribution to poleward MSE transport due to lower occurrence frequency, *global-specific* and DL ARDTs detect stronger AR events that transport significantly more MSE poleward, often 3 to 5 times their corresponding occurrence frequency (Figure 2b). Due to their lower AR occurrence, *polar-extreme* ARDTs contribute only 1%–4% of poleward MSE transport. The Wille-vIVT ARDT, based on the meridional IVT detection measurement, is more efficient in transporting MSE poleward, contributing 4 to 5 times their occurrence frequency (Figure 2b).

Consistent with the meridional variability of AR occurrence frequency in Figure 1a, ARDTs based on absolute thresholds, including the *polar-constrained* and *global-specific* ARDTs, exhibit rapid decreases in AR-related poleward MSE transport in spring, fall and winter. In contrast, during summer, their contribution values decrease more slowly. Similarly, DL ARDTs limit the detected AR occurrences to only the strongest events, which significantly impacts the results over higher latitudes. Percentile-only, grid point- and seasonal-dependent ARDTs (i.e., Purdue-85th-IVT and *polar-extreme* ARDTs) display a slower decrease in AR contribution to MSE transport with latitude than the polar-constrained and global-specific ARDTs. The Gorodetskaya ARDT using the temperature-adjusted saturated IWV also shows a slower decline in their contribution north of 70°N. It is noted that in summer, the Purdue-85th-IVT ARDT corresponds to a similar or even smaller portion of poleward MSE transport compared to other *polar-constrained* ARDTs, such as the Guan-Waliser ARDT. The Gorodetskaya ARDT shows comparable magnitudes to those using *global-specific* and *polar-extreme* ARDTs.

Overall, the seasonality in AR occurrence frequency (Figure 1a) largely determines the seasonality in AR contributions to poleward MSE transport, $\frac{\text{AR\_MSET}_P}{\text{MSET}_P}$ (Figure 2a). For example, Purdue-85th-IVT and *polar extreme* ARDTs exhibit minimal seasonality in $\frac{\text{AR\_MSET}_P}{\text{MSET}_P}$ due to their percentile-only-based, seasonally dependent algorithms. In contrast, *polar-constrained* ARDTs exhibit significant seasonality, with the largest $\frac{\text{AR\_MSET}_P}{\text{MSET}_P}$ occurring in summer and less in cold seasons. The peak in summer is attributed to their highest AR occurrence frequency in summer (Figure 1a) and corresponding large AR_MSET$_P$ (Figure S1a in Supporting Information S1), alongside decreased total climatological MSET$_P$ (Figure S1a in Supporting Information S1) caused by the weakened meridional temperature gradient between mid- and high-latitudes in summer. The Gorodetskaya ARDT exhinits the opposite seasonality, with a pronounced minimum in summer. *Global-specific* and DL ARDTs tend to show smaller seasonality, with relatively larger AR contributions in fall due to the larger AR occurrence frequency and corresponding larger AR_MSET$_P$ in this season (Figure S1a in Supporting Information S1).

At 70°N, the longitudinal distribution of $\frac{\text{AR\_MSET}_P}{\text{MSET}_P}$ in Figure 2c closely mirrors that of AR occurrence frequency in Figure 1b for most ARDTs (except for Purdue-85th-IVT and *polar-extreme*). This similarity indicates that AR occurrence frequency largely determines their contribution fraction to total poleward MSE transport, particularly for absolute-based ARDTs. Specifically, during non-summer seasons, these ARDTs show the largest AR contributions to poleward MSE transport primarily over the Arctic Atlantic (extending to Barents-Kara Seas) and Arctic Pacific sectors, which align with the regions of highest AR occurrence frequency observed in Figure 1b, and consequently, the highest AR_MSET$_P$ observed in Figure S1b of Supporting Information S1. In addition to these Arctic oceanic sectors, there are localized maxima as total MSET$_P$ pathways, such as the western edge of Greenland, Alaska, and East Siberia as depicted in Figure S1b of Supporting Information S1. In these areas, ARs only transport moderate to lesser amounts of MSE poleward, resulting in smaller contributions visible in Figure 2c. In summer, the reduced meridional temperature gradient between mid- and high-latitudes leads to decreased longitudinal variability in total MSET$_P$ (Figures S1b and S2b in Supporting Information S1). Moreover, the longitudinal variability of AR occurrence frequency (Figure 1b) is also reduced due to the weakening of storm tracks over oceanic regions and strengthening of cyclonic storms over continents (Serreze et al., 2009). Consequently, this results in less focused MSE transport, shown as smaller longitudinal variability in AR_MSET$_P$ (Figure S1b in Supporting Information S1) and $\frac{\text{AR\_MSET}_P}{\text{MSET}_P}$ (Figure 2c), compared to other seasons. In contrast, the percentile-only based ARDTs (i.e., Purdue-85th-IVT and *polar extreme*) display little variability in the longitudinal distribution of AR occurrence frequency (Figure 1b) due to their grid-point dependent detection algorithm. However, they exhibit greater variability in AR contribution to MSE transport (Figure 2c) due to the large spatial variability of total MSET$_P$ and resultant AR_MSET$_P$ (Figure S1b in Supporting

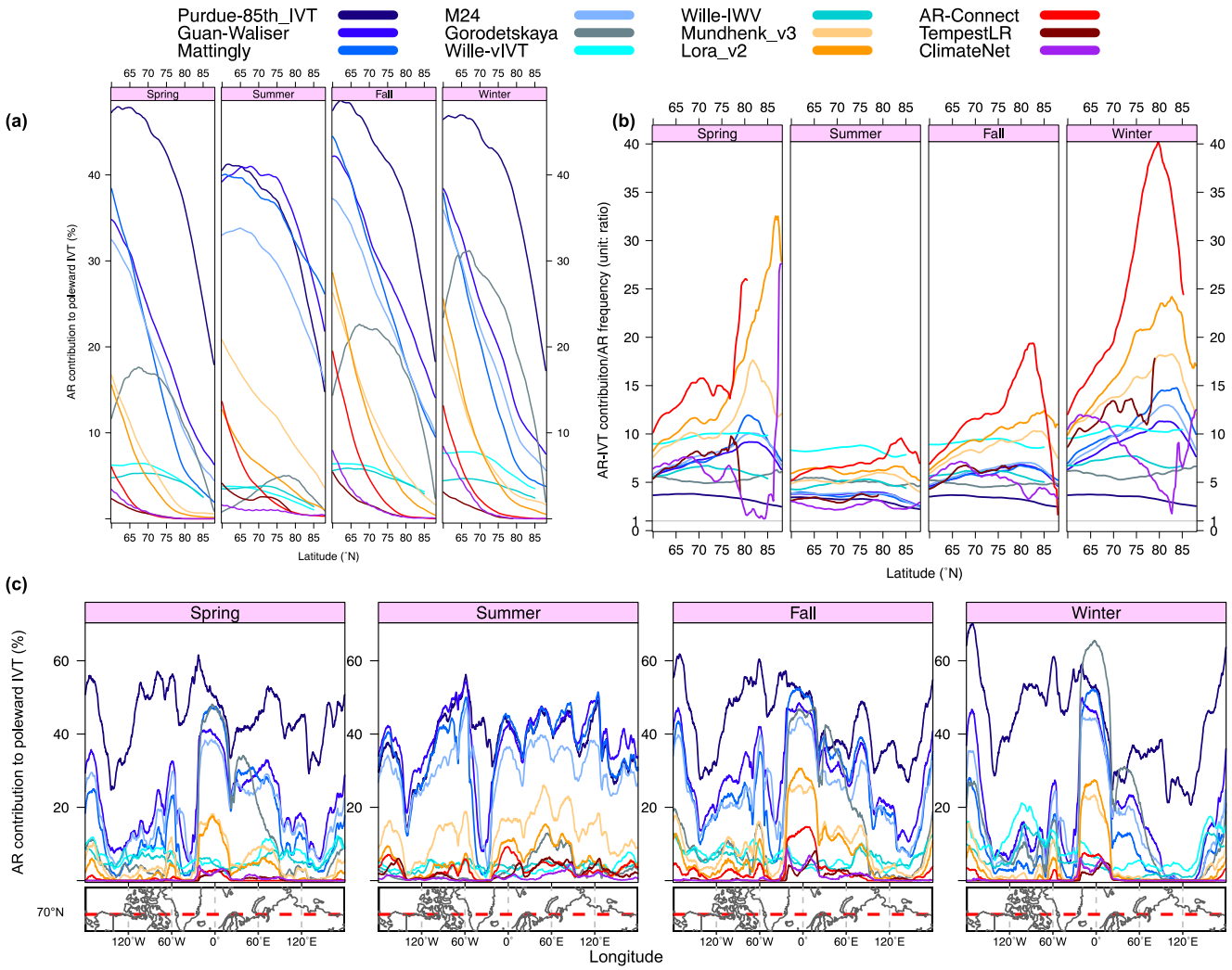

Figure 3. (a) Zonal distribution of AR contribution to total poleward IVT ($\frac{AR\_IVT_P}{IVT_P}$, unit: %) from 60°N to 88°N during each season (Spring: Mar–May, Summer: Jun–Aug, Fall: Sep–Nov, Winter: Dec–Feb) from 2000 to 2019 using 12 ARDTs. (b) Zonal distribution of the ratio of AR contribution to total poleward IVT (panel (a)) to AR occurrence frequency (Figure 1a) from 60°N to 88°N during each season. (c) Longitudinal distribution of AR contribution to total poleward IVT ($\frac{AR\_IVT_P}{IVT_P}$, unit: %) at 70°N during each season detected by all 12 ARDTs. An Arctic map showing the region crossing the 70°N (red dotted line) is displayed at the base of each panel.

Information S1). The *polar-specific ARDTs* using the 85th percentile climate thresholds, with or without an absolute threshold, agree on AR contribution in summer, except for Greenland (with Purdue-85th-IVT as an outlier of 20% contribution).

Overall, at 70°N, most ARDTs (except DL and TempestLR ARDTs) display AR contributions to poleward MSE transport at a rate more than twice to over six times their AR occurrence frequency, except in regions like the Beaufort Sea in summer and northeast Eurasian continent in spring, fall and winter where lower AR occurrence frequency result in lesser contributions. In contrast, over the Canadian Archipelago, AR contributions to poleward MSE transport can exceed four times their corresponding AR frequency, which can be attributed to the prevailing meridional southward meridional transports (Figure S2b in Supporting Information S1) and overall smaller poleward transports there (Figure S1b in Supporting Information S1), highlighting the significant role ARs play in these regions.

4.2. AR Contributions to Atmospheric Moisture Transport

ARs play a more significant role in transporting moisture poleward (Figure 3) compared to their role in poleward MSE transport (Figure 2), as indicated by larger contribution percentages. There is a wide range of AR

contributions to poleward IVT (0%∼49% in Figure 3a) as a result of the large range of AR occurrence frequency (0%∼14% in Figure 1a) due to different AR detection criteria. Poleward of 60°N (Figure 3a), the Purdue-85th-IVT detects more ARs and accounts for the highest poleward IVT, ranging from 15% to 49%, which is approximately 2–4 times the corresponding AR occurrence frequency (Figure 3b). *Polar-constrained* ARDTs, which detect fewer but stronger ARs, contribute 2%–44% of total poleward IVT, corresponding to 2 to 15 times their occurrence frequency. ARs detected using the Gorodetskaya ARDT contribute 0.8%–31% of the total poleward IVT, which is approximately 4–7 times their occurrence frequency. Other ARDTs emphasize extreme events, which minimizes their total contribution to poleward IVT due to low occurrence frequency. For instance, *polar-extreme* ARDTs contribute 1%–8% of total poleward IVT, which is 4–11 times their corresponding frequency. *Global-specific* and DL ARDTs have contributions range from 0% to 29% for Mundhenk_v3, Lora_v2, and AR-Connect, and 0%–8% for TemestLR and DL ARDT, exceeding their occurrence frequency by more than 5 times.

AR occurrence frequency (Figure 1a) largely determines AR contributions to climatological poleward IVT, exhibiting similar seasonality and meridional variability (Figure 3a), consistent with Figure 1a. Percentile-based ARDTs (i.e., Purdue-85th-IVT and *polar extremes*) exhibit little seasonality and a gradual meridional decrease, except for a sharp drop-off in $\frac{\overline{\text{AR\_IVT}_P}}{\overline{\text{IVT}_P}}$ at higher latitudes for Purdue-85th_IVT due to the rapid decrease in AR frequency. *Polar-constrained* ARDTs display considerable longitudinal variability and prominent seasonality, with the largest contributions in summer and fall due to the highest AR occurrence frequency and corresponding largest AR_IVT_P (Figure S3a in Supporting Information S1). In contrast, the Gorodetskaya ARDT displays the opposite seasonality, with a minimum in summer. *Global-specific* and DL ARDTs tend to show smaller seasonality due to overall smaller magnitudes, with relatively larger AR contributions in fall, consistent with the larger AR occurrence frequency and correspondingly larger AR_IVT_P during this season.

As discussed in Figure 1a, absolute threshold-based ARDTs (such as *polar-constrained* and *global-specific* ARDTs), which impose more restrictive climate criteria, detect fewer ARs in the Arctic, with a minimum in higher latitudes during cold seasons. This is evident in Figure S3a of Supporting Information S1 where the minimum climatological IVT_P makes it difficult to satisfy the absolute thresholds, limiting AR detection and leading to a sharp decrease in the AR occurrences frequency in the higher Arctic during the cold seasons. Although fewer ARs are detected, these ARs are extreme and contribute to total poleward moisture transport more than five times their corresponding occurrence frequency, with even higher ratios at higher latitudes in cold seasons (Figure 3b). In summer, *polar-constrained* ARDTs display a gradual decrease of detected ARs in the lower latitudes of the Arctic (Figure 1a) and a corresponding gradual decrease in AR contributions to poleward moisture transport (Figure 3a). This is because, in summer, higher climatological IVT_P (Figure S3a in Supporting Information S1) often exceeds the 100 or 150 kg m^{-1} s^{-1} absolute thresholds, with grid point-dependent 85th percentile climate thresholds dominating the detection criteria of *polar-constrained* ARDTs.

Figure 3c shows the longitudinal distribution of AR contributions to total poleward IVT ($\frac{\overline{\text{AR\_IVT}_P}}{\overline{\text{IVT}_P}}$) at 70°N for each of the 12 ARDTs. In general, the longitudinal distribution of AR occurrence frequency at 70°N (Figure 1b) significantly influences the distribution of their total contributions to poleward IVT, with exceptions for Purdue-85th-IVT and *polar-extreme* ARDTs. For most ARDTs, during cold seasons, the maximum AR contributions are consistently located over the Arctic Atlantic and Pacific sectors, coinciding with the maximum IVT_P and AR_IVT_P pathways observed in Figure S3b of Supporting Information S1 and the end of the mid-latitude storm tracks, indicating a strong connection between mid-latitude storms and Arctic ARs, which play a significant role in transporting moisture poleward over the primary IVT_P pathways to the Arctic. Over these regions, ARs contribute to 47%–66% of total IVT_P for the Gorodetskaya and *polar-constrained* ARDTs, 8%–31% for *global-specific* ARDTs, and 9% for DL ARDT, more than three times their corresponding AR occurrence frequency. Baffin Bay, another IVT_P pathway seen in Figure S3b of Supporting Information S1, receives secondary local maximum AR contributions, which can exceed more than five times their corresponding occurrence frequency. In the summer there is less longitudinal variability in AR occurrence frequency (Figure 1b) and AR contribution to poleward IVT (Figure 3c) compared to the other seasons. Weakened storm activity over the Arctic Atlantic sector in summer leads to slightly reduced ARs and AR contributions to poleward IVT. Additionally, total IVT_P and AR_IVT_P are higher almost everywhere in summer (Figure S3b in Supporting Information S1), particularly over continents, although it remains minimal over Greenland, contributing to the reduced longitudinal variability in AR contribution to poleward IVT in summer (Figure 3c). Larger IVT_P and AR_IVT_P in summer are likely due to

greater moisture from increased evaporation and intensified storm activity (such as cyclone activity) that increases the advection of moisture over northern Eurasia and Canada (Dufour et al., 2016; Serreze et al., 2009; Tilinina et al., 2013). As a result, in summer, higher AR occurrence frequencies lead to a greater total contribution to poleward IVT, especially over the Eurasian continent, while minimal contributions are noted over Greenland and the Beaufort Sea due to fewer detected ARs (Figure 1b) and less AR_IVT$_P$ (Figure S3b in Supporting Information S1), respectively. Note that the maximum magnitudes of ARs and associated AR_IVT$_P$ detected by the Gorodetskaya ARDT over the Eurasian continent in summer are much lower than those over the Atlantic sector during non-summer seasons.

Although there is little longitudinal variability in AR occurrence frequency (Figure 1b) for percentile-only-based ARDTs (Purdue-85th-IVT and *polar-extreme*), the total moisture they carry shows large longitudinal variability due to the large variability of climatological total IVT$_P$ (Figure S3b in Supporting Information S1), therefore distinct longitudinal variability in AR contributions to poleward IVT (Figure 3c). Purdue-85th-IVT shows agreement with *polar-constrained* ARDTs over oceans, particularly the Arctic Atlantic sector, due to similar detected AR occurrence frequencies, but larger contributions over the Arctic Pacific sector. In summer, Purdue-85th-IVT and *polar-constrained* ARDTs largely align in AR contributions except for Greenland. The Gorodetskaya ARDT generally agrees with the *polar-constrained* ARDTs over the Atantic sector and into the Barents Sea during non-summer seasons, but shows much lower magnitudes over land and across all regions during summer. *Polar extreme* ARDTs, especially Wille-vIVT, display significant longitudinal variability due to their poleward IVT-based AR detection measurements, with higher contributions over the Eurasian continent in spring and fall, and the Canadian Archipelago in spring, fall, and winter. For the primary IVT_P pathways over Arctic Atlantic and Pacific sectors, their role in transporting moisture poleward does not seem to be as important as results derived from other ARDTs.

Overall, total latent heat transport (L_v × IVT) constitutes only a small part of the total MSE transport, comprising about 1% when comparing their magnitudes as shown in Figures S1 and S3 of Supporting Information S1. ARs play a more significant role in transporting moisture poleward than in MSE transport, as evidenced by the higher percentage contribution of ARs to the total poleward moisture transport (Figure 3) compared to poleward MSE transport (Figure 2). Particularly, their maximum contributions both occur over the primary IVT pathway in the Arctic Atlantic sector, owing to the maximum AR occurrence frequency in that region.

5. AR Impacts on Surface Downward Longwave Radiation and Surface Total Precipitation

As stated, many previous Arctic AR studies highlight the significant impacts of ARs on LWD and surface precipitation. These impacts influence the subsequent surface radiation and energy budgets, leading to enhanced surface warming and sea ice decline over the Arctic during the boreal winter (e.g., Hegyi & Taylor, 2018; Woods & Caballero, 2016; P. Zhang et al., 2023). In this study, we quantify the relationship between AR occurrences, as identified by various ARDTs, and their associated impacts on LWD and precipitation in the Arctic. Our focus is on the average LWD anomalies during AR events in each season and their total integrated AR LWD contribution to seasonal climatological LWD. The average anomalies of LWD for AR events are calculated by first determining 3-hourly anomalies from 2000 to 2019 relative to the 20-year climatological mean for each day of the year and then averaging these anomalies at each grid point across all AR occurrences for each season. Using the same approach, we also calculate the average AR-related total precipitation anomalies and quantify the AR contribution to the seasonal climatological precipitation totals.

5.1. AR-Related Surface Downward Longwave Radiation Anomalies and Their Seasonal Climatological Contributions

The average AR-related LWD anomalies for each of the 12 ARDTs during each season are shown in Figure 4a. As expected, all 12 ARDTs show that ARs produce significant positive LWD anomalies across the entire Arctic, likely due to enhanced water vapor content and cloud formation associated with ARs. More restrictive criteria, such as *global-specific* ARDTs, tend to detect fewer but more extreme ARs in the Arctic, resulting in larger average AR-LWD anomalies. Less restrictive ARDTs, such as Purdue-85th-IVT, detect both extreme and moderately intense ARs, leading to smaller average AR-LWD anomalies. According to the 12 ARDTs, the AR LWD anomalies range from a minimum of 10–43 W m^{-2} in summer to a maximum of 38–116 W m^{-2} in winter.

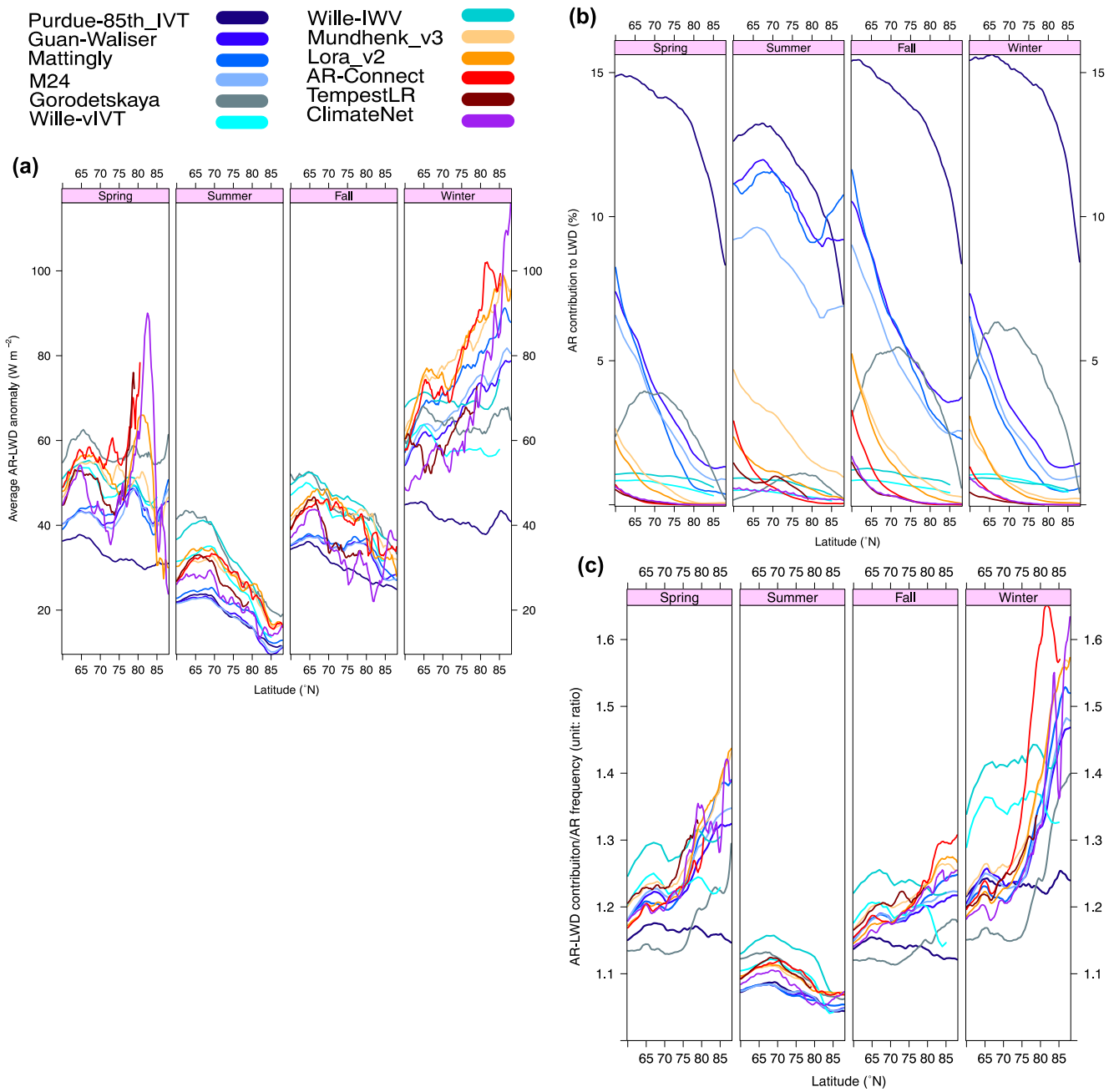

Figure 4. (a) Zonal mean distribution of average LWD anomalies (unit: W m^{-2}) during AR occurrences across latitudes from 60°N to 88°N during each season from 2000 to 2019 using 12 ARDTs. (b) Zonal mean distribution of AR contribution to seasonal climatological LWD (unit: %) cross latitudes from 60°N to 88°N during each season from 2000 to 2019 using 12 ARDTs. (c) Zonal mean distribution of the ratio of AR contribution to total LWD (panel (b)) to AR occurrence frequency (Figure 1a) from 60°N to 88°N during each season.

All 12 ARDTs, no matter absolute- or percentile-based, or temperature adjusted IWV-based- display significant seasonality, with the maximum AR LWD anomalies occurring in winter and the minimum in summer. Spring and fall have intermediate values of AR LWD anomalies. As discussed in C. Zhang et al. (2025) the seasonality of LWD anomalies associated with Arctic ARs may be related to previous research indicating that longwave cloud forcing is most sensitive to clouds with low liquid water paths, with this sensitivity decreasing as the liquid water path increases (Chen et al., 2006). Arctic clouds typically contain lower amounts of liquid water during the winter. Any increase in this low-content cloud liquid water due to Arctic ARs results in a more significant LWD anomaly. Additionally, during winter, the influence of clear-sky LWD on surface warming is more pronounced compared

to summer, due to the dry and cold conditions prevalent in the Arctic (R. Zhang et al., 2021). Under these conditions, ARs enhance water vapor transport, which increases clear-sky LWD by intensifying the greenhouse effect even in the absence of clouds. As a result, winter AR LWD is likely more influenced by clear-sky LWD, making its contribution to surface warming particularly significant during cold seasons.

Percentile-only based ARDTs, such as Purdue-85th-IVT and Wille-vIVT, show little latitudinal variability in LWD anomalies during the winter. North of 60°N, their anomaly values range from 38 to 46 W m^{-2} for Purdue-85th-IVT and from 56 to 64 W m^{-2} for Wille-vIVT (Figure 4a). While there are few differences in the detected AR occurrences between Wille-vIVT and Wille-IWV, the average AR-LWD anomalies are larger and show distinct meridional variability when using the Wille-IWV, with values ranging from 67 to 74 W m^{-2} poleward of 60°N poleward. This might be due to IWV-based ARDTs emphasizing moisture content alone, as increases in IWV are correlated with increases in LWD (Wille et al., 2019). Similarly, IWV-based-Gorodetskaya ARDT is associated with larger LWD anomalies in spring and fall compared to the polar-constrained ARDTs, despite detecting a similar frequency of ARs north of 70°N. Other ARDTs display sharp increases in LWD anomalies with latitude, ranging from 49 to 62 W m^{-2} at 60°N to the maximum of 73–116 W m^{-2} at higher latitudes. As seen in Figure 1a, most ARDTs, particularly those based on absolute thresholds, detect lower AR occurrence frequencies, with a minimum over the higher Arctic. However, as the temperature and moisture decrease to their minimum in the central Arctic, any ARs detected by these absolute-threshold-based ARDTs are extremely intense, producing the largest LWD anomalies in the climatological minimum LWD environment. In contrast, during summer when climatological LWD is at its maximum, although there is a large difference in AR occurrence frequencies between polar-specific ARDTs using the 85th percentile climate thresholds and other ARDTs (Figure 1a), their AR-LWD anomalies are similar and display a smaller range. Gorodetskaya ARDT-related summer LWD anomalies (18–43 W m^{-2}) resemble thoese derived using the Wille-IWV ARDT and are larger than those from Wille-vIVT ARDT. All 12 ARDTs show that anomaly values range from 22 to 41 W m^{-2} at 60°N, gradually increasing to a local maximum of 23–43 W m^{-2} between 63 and 69°N, then decreasing to a minimum of 10–18 W m^{-2} at around 85°N. Most ARDTs display larger AR-LWD anomalies in spring (24–90 W m^{-2}) compared to fall (22–53 W m^{-2}).

Although Figure 4a shows large positive AR-LWD anomalies; the AR contribution to seasonal LWD ranges from less than 1% to over 15% of the seasonal climatological LWD, depending on the AR detection methods used, as seen in Figure 4b. The contribution patterns align with the AR occurrence frequency shown in Figure 1a, indicating that AR occurrence frequency strongly influences their total contribution to climatological surface LWD impacts. The ratio of AR contribution to seasonal LWD to AR occurrence frequency is always greater than 1 and ranges from about 1.04 to greater than 1.5 (Figure 4c) indicating that AR contribution to seasonal LWD ranges from 4% to over 50% more to seasonal LWD than expected based on their AR occurrence frequency.

The results in Figure 4 reveal that ARDTs with large AR-LWD anomalies (Figure 4a), due to the extreme nature of their infrequently detected ARs, result in a small overall contribution to seasonal LWD (Figure 4b). ARDTs with larger AR occurrence frequency and smaller AR-LWD anomalies make a larger overall contribution to seasonal LWD. For example, *polar-specific* ARDTs using the 85th percentile climate thresholds with higher AR occurrence frequencies (Figure 1a) and smaller AR-LWD anomalies (Figure 4a) exhibit larger AR contributions to seasonal LWD (Figure 4b). The Purdue-85th-IVT, which does not use any absolute thresholds, detects the highest AR occurrence frequency but has the smallest average AR-LWD anomalies. It accounts for a maximum contribution of 7%–16% to the seasonal climatological LWD, with minimal seasonality. These contribution percentages are about 1.04–1.3 times their corresponding AR occurrence frequencies (Figure 4c). *Polar-constrained* ARDTs with additional 100–150 kg m^{-1} s^{-1} absolute thresholds show larger contributions of 6%–12% in summer, with percentage values similar to their AR occurrence frequency, although they have smaller AR-LWD anomalies in this season. During winter, although the largest AR-LWD anomalies are observed, their least frequent occurrences result in accumulated contributions that decrease from around 6%–7% at 60°N to 0.5%–1% in the higher Arctic, which is around 1.5 times their AR occurrence frequency (Figure 4c). Still, the Gorodetskaya ARDT shows the opposite seasonality, with the highest contribution in winter (0.4%–6%) and the lowest in summer (0.2%–1.1%), corresponding to 1.1–1.4 times and 1.1times of their frequences, respectively. *Global-specific* and DL ARDTs tend to detect extreme ARs with intense AR-LWD anomalies. Their overall contribution percentages are smaller, ranging from the maximum of 1.5%–5% at 60°N in fall to nearly 0.0% in higher Arctic due to fewer detected AR events. Consequently, their seasonality is weaker compared to polar-

constrained ARDTs. Although *polar extreme* ARDTs detect larger average AR-LWD anomalies, their total contributions range only from 0.1% to 1.3% with little seasonality due to the smaller AR occurrence frequency.

To complement the analysis of AR-related LWD impacts, we present spatial distributions (Figures S5–S16 in Supporting Information S1) of 20-year averaged AR-induced LWD anomalies and their contribuitons to seasonal climatological LWD across the Arctic (north of 60°N) for each of the 12 ARDTs. The over spatial features are well captured in Figures 4a and 4b, with some spatial details. In winter, the largest anomalies appear over the central Arctic Ocean extending to both the Eurasian and North American continents, especially for *polar-constrained* ARDTs that detect fewer but most intense ARs. *Global-specific* ARDTs using stricter absolute thresholds tend to miss ARs in these coldest regions, resulting in non-detection of ARs. Localized LWD anomaly maxima are observed along the sea ice margins, particularly from the Greenland Sea to the Barents-Kara Seas. These maxima are most prominent in winter for percentile-only based ARDTs (e.g., Purdue_85th-IVT, Wille-vIVT), and they persist into spring for all polar-specific ARDTs and some global-specific ARDT (such as Lora_v2 and Mundhenk_v3). These regions coincide with areas of rapid sea ice decline and seasonal onset of sea ice melt, suggesting these ARDTs may better capture radiatively impactful ARs relevant to potential initiation or acceleration of sea ice melt. In summer, spatial differences between ARDTs largely diminish, but increased AR frequency lead to greater overall contributions to seasonal LWD across the Arctic.

5.2. AR-Related Surface Total Precipitation Anomalies and Their Seasonal Climatological Contributions

The average AR-related total surface precipitation anomalies for each of the 12 ARDTs during each season are shown in Figure 5a, with spatial distributions of the 20-year average anomalies across the entire Arctic presented in panel (a) of Figures S17–S28 of Supporting Information S1. As expected, all ARDTs indicate enhanced precipitation during AR events throughout the Arctic, reflecting the strong thermodynamic characteristics of AR. However, the magnitude and spatial coverage of these precipitation anomalies vary considerably among ARDTs due to differences in detection criteria.

Global-specfic ARDTs, which apply more restrictive thresholds, typically detect fewer but more intense ARs, leading to higher precipitation anomalies, ranging 0.13–1.3 mm/hr (Figure 5a), but limited spatial coverage, as shown in Figures S17–S28 of Supporting Information S1. In contrast, *polar-specific* ARDTs using 85th percentile climate thresholds capture a broader range of AR intensities, including more frequent and moderate events, yielding wider spatial coverage but lower average anomalies (0.04–0.3 mm/hr). In spring, fall and winter, *polar-extreme* and the Gorodetskaya ARDTs exhibit similarly high precipitation anomalies south of 65°N-comparable to those from *global-specfic* ARDTs-while their anomaly magnitudes drop north of 65°N, aligning more closely with those from *polar-specific* ARDTs. In summer, however, both *polar-extreme* and the Gorodetskaya ARDT show larger precipitation anomalies, likely due to their detection of fewer, more intense AR events. Although the DL-based ClimateNet ARDT detects ARs with similar frequency to *global-specific* ARDTs, its associated with smaller precipitation anomalies. This suggests that while AR frequency may align, the detected ARs differ in intensity and structure, influencing the resulting precipitation impacts.

Compared to AR-related LWD anomalies, the seasonality of AR-induced precipitation anomalies is less pronounced. While winter and fall generally exhibits slightly higher anomalies and spring and summer slightly lower, the contrast is modest. This suggests that, unlike radiative impacts, AR-induced precipitation is less sensitive to cold, dry background conditions. The modest increase in winter anomalies likely reflects enhanced baroclinicity and stronger poleward moisture fluxes, often resulting in snowfall. In summer, the background atmosphere is moister and the intensity of more frequent ARs is somewhat reduced, the relative anomaly magnitude is limited. Despite weaker seasonality, AR-related precipitation shows stronger latitudinal variability, especially for *global-specific* ARDTs with more restrictive thresholds. As shown in Figures S17–S28 of Supporting Information S1, regions such as the Bering Sea into interior Alaska and Siberia, the Norwegian Sea toward the western coast of Norway and the Greenland Sea exhibit strong AR-induced precipitation anomalies—particularly in winter—corresponding to storm tracks and enhanced moisture transport. In particular, local maxima are evident over major mountainous regions including Alaska, the Scandinavian Mountains, eastern and western Greenland, and parts of Siberia, largely driven by strong orographic lifting.

Although AR-related precipitation anomalies may not always be extreme in magnitude, ARs can account for a substantial portion of the total precipitation, with contributions ratios often far exceeding their occurrence frequencies. For instance, in summer, *polar-specific* ARDTs using 85th percentile climate thresholds show that ARs

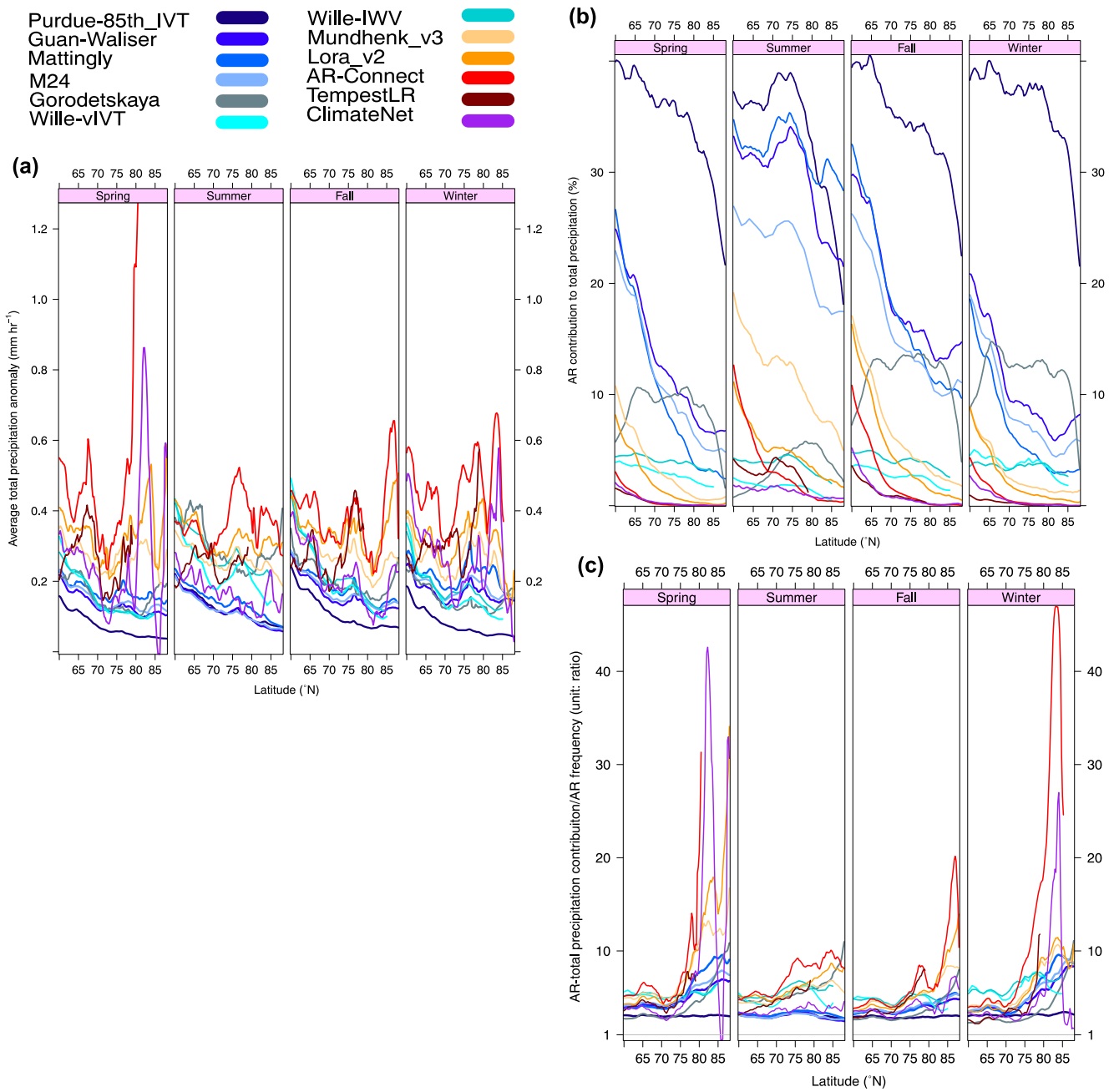

Figure 5. (a) Zonal mean distribution of average total precipitation anomalies (unit: mm hr^{-1}) during AR occurrences across latitudes from 60°N to 88°N during each season from 2000 to 2019 using 12 ARDTs. (b) Zonal mean distribution of AR contribution to seasonal climatological total precipitation (unit: %) cross latitudes from 60°N to 88°N during each season from 2000 to 2019 using 12 ARDTs. (c) Zonal mean distribution of the ratio of AR contribution to total precipitation (panel (b)) to AR occurrence frequency (Figure 1a) from 60°N to 88°N during each season.

account for 17%–39% of total seasonal precipitation (Figure 5b), with contribution ratios 2.5–3.6 times their occurrence frequencies (Figure 5c). In non-summer seasons, although ARs are less frequent, their contribution still range from 2.4% to 41%, corresponding to 3–10 times their occurrence frequency. The Gorodetskaya ARDT displays an opposite seasonality, with the lowest contributions in summer (0.8%–5.8%) and highest in non-summer seasons (1.6%–14.8%), consistent with its seasonal ARs detection variation. These contribution represent 4–11 times the expected precipitation based on AR frequency in summer and 2–11 times in winter. *Global-specific* ARDTs, although detecting ARs with the largest precipitation anomalies, contribute less to seasonal totals due to their low detected occurrence frequency. Their overall contributions range from 0% to 19%,

Table 2
Summary of the Performance of 12 AR Detection Algorithms Included in the Intercomparison

		AR frequency (zonal mean occurrence)	Poleward MSE transport contribution	Polward IVT contribution	LWD impact	Precipitaion impact	Seasonality and latitudinal varaiblitiy
Polar-Specific	Purdue-85th IVT	Highest (up to 13.6%)	Highest (up to 33%)	Highest (up to 49%)	Smallest anomalies, largest total LWD contribution (7%–16%)	Smallest anomalies, largest total precipitation (up to 41%)	Little
	Guan-Waliser Mattingly M24	Higher (up to 11% in summer)	Higher (up to 29% in summer)	Higher (up to 45% in summer)	Large anomalies, modest total contribution (up to 12% in summer)	Large anomalies, modest total contribution (up to 35% in summer)	Large
	Gorodetskaya	High in cold seasons (2%–5.5%), min in summer (<1%)	High in cold seasons (~12%), min in summer (<2.5%)	High in cold seasons (~31%), min in summer (<5%)	Large anomalies, modest total contribution (summer min, <1.1%)	Large anomalies, modest total contribution (summer min, <5.8%)	Distinct seasonality, min in summer, large in cold seasons
	Wille-vIVT Wille-IWV	Lowest (<1%)	Lower (<4%)	Lower (<8%)	Large anomalies, small total contribution (<1.3%)	Large anomalies, small total contribution (<5%)	Little
Global	Mundhenk v3 Lora v2 AR-Connect TempestLR	Lowest (0.0%–4.6%)	Lower (<16%)	Lower (<29%)	Largest anomalies (>100 W m^{-2} in winter), lowest total contribution (<5%)	Largest anomalies, lowest total contribution (<19%)	Large
DL	ClimateNet	Lowest (<1.5%)	Lowest (<4%)	Lowest (<8%)	Large anomalies, lowest contribution (<1.7%)	Large anomalies, lowest contribution (<5%)	Large

yet in some high Arctic regions, contributions can be up to 20 times what would be expected based on AR occurrence frequency, such as the Lora_v2 ARDT in spring (Figure 5c), highlighting the disproportionate impact of rare, extreme AR events. Nevertheless, these events are extremely infrequent, occurring less than 0.05% of the time-equivalent to only a few hours, or a single AR event in spring over the 20 years.

While ARs are relatively infrequent, they are disproportionately responsible for precipitation across the Arctic, particularly over the Atlantic and Pacific oceanic sectors during cold seasons, consistent with climatological storm tracks, and across broader regions in summer (Figures S17–S28 in Supporting Information S1). Contribution ratios exceeding 3 across most ARDTs and large portions of the Arctic demonstrate that ARs deliver significantly more precipitation than would be expected based on their occurrence frequency alone. ARDTs that capture a broader spectrum of AR intensities—especially *polar-specific* ARDTs —consistently yield more stronger and spatially extensive seasonal contributions. These results highlight the importance of the selected ARDTs when quantifying AR-related hydro-meteorological impacts in the Arctic climate system.

6. Discussions and Conclusions

This study evaluates the performance of 12 prevailing ARDTs in detecting AR occurrence frequency (Section 3), AR atmospheric heat (represented by MSE) and moisture (IVT) transport (Section 4), and surface LWD and precipitation impacts (Section 5) in the Arctic, using ERA5 reanalysis data from 2000 to 2019. The performance of 12 ARDTs is concisely summarized in Table 2. These ARDTs are divided into three categories based on their climate thresholds and their application to either polar or global regions. *Polar-specific* ARDTs, which include both percentile only based ARDTs like Purdue-85th-IVT, *polar-extreme*, Gorodetskay ARDT using temperature-adjusted saturated IWV thresholds, as well as *polar-constrained* ARDTs that use additional absolute IVT thresholds (100 or 150 kg m^{-1} s^{-1}) to supplement the 85th percentile climate thresholds. *Global-specific* ARDTs,

originally designed for mid-latitudes, apply more restrictive absolute or relative thresholds. DL ARDTs form a separate category based on deep learning AR detection methods. This classification reduces variability within each category while highlighting significant contrasts between them. For brevity, nuanced criteria such as AR geometry, direction, or temporal criteria are not discussed, as they are secondary to climate threshold criteria for AR index generation and corresponding climatology statistics (C. Zhang et al., 2021).

AR occurrence frequency varies widely in the Arctic, from less than 1% to over 13%, depending on the ARDT used with AR frequency decreasing with latitude (Figure 1a). This variability leads to differences in contributions to poleward MSE transport (<1% to >33% in Figure 2a) and poleward IVT (<1% to >49% in Figure 3a). *Polar-specific* ARDTs using the 85th percentile climate thresholds are typically associated with the highest AR occurrence frequency and the largest contributions to poleward MSE transport and IVT.

There is substantial agreement between the Purdue-85th-IVT (which does not use any absolute thresholds) and *polar-constrained* ARDTs that do use absolute thresholds during the summer season (except over Greenland, as seen in Figures 1b, 2b and 3b). However, significant differences arise during other seasons, particularly in winter (Figures 1a, 2a and 3a). This discrepancy is mainly because the 85th percentile climate threshold drops below 100 kg m^{-1} s^{-1} in most of the Arctic domain during non-summer seasons (especially winter) and in Greenland during summer, resulting in lower AR occurrence frequency and lower contributions to poleward moisture and heat transport in the *polar-constrained* ARDTs. Note that the M24 ARDT is based on the Guan-Waliser detection algorithm with slight modification. However, due to its use of coarser spatial and temporal resolution, it tends to detect fewer ARs, especially in summer, highlighting the potential advantage of finer-resolution data for more accurately capturing the spatial structure and temporal variability of Arctic ARs. Future investigation is warranted to fully understand how resolution differences affect AR detection, especially in the context of climate modeling, where accurate representation of ARs is critical. Other ARDTs, due to their more restrictive climate thresholds, detect much lower AR occurrence frequency (<5%) and correspondingly smaller contributions to poleward MSE transport (<16%) and IVT (<29%).

In cold seasons (fall, winter, and spring), most ARDTs (except for Purdue-85th-IVT and *polar-extreme* ARDTs) show that the highest AR occurrence frequency (Figure 1b) and AR contributions to the transports of MSE (Figure 2b) and moisture (Figure 3b) occur over the Atlantic sector. This region hosts the primary IVT pathway (Figure S3b in Supporting Information S1), associated with the Atlantic mid-latitude storm track, highlighting a strong connection between mid-latitude storms and Arctic ARs, which significantly contribute to poleward MSE and moisture transport. The next largest AR contributions to poleward MSE transport and IVT are over the Arctic Pacific and Baffin Bay. The use of percentile-only climate thresholds in the Purdue-85th-IVT and *polar-extreme* ARDTs result in a relatively uniform longitudinal distribution of AR occurrence frequency (Figure 1b) that does not isolate the linkage between AR occurrence and mid-latitude storms seen in the other ARDTs. In summer, most ARDTs show that ARs occur more frequently across almost all of the Arctic, particularly over the continents, while the Atlantic sector is less prominent compared to other seasons, likely due to increased mid-latitude cyclonic storms over continents but reduced storm activity over the Arctic Atlantic sector in summer (Dufour et al., 2016; Tilinina et al., 2013). Consequently, overall higher contributions to poleward MSE transport and IVT occurred in summer. Greenland consistently shows lower AR occurrence frequency and smaller contributions throughout the year (except for Purdue-85th-IVT), potentially due to the minimum climatological IVT or IWV that limits AR detection over Greenland. Additionally, the prevailing equatorward moisture transport over the Greenland-Denmark Strait (Figure S4 in Supporting Information S1) leads to reduced poleward moisture transport (Figure S3 in Supporting Information S1), further limiting AR detection, particularly in summer. Notably, the Gorodetskaya ARDT shows an opposite seasonality, with higher AR frequency in cold seasons (maximum in winter, particularly in Atlantic sector), and minimum in summer. This is distinct seasonality may stem from its temperature-adjusted saturated moisture threshold. Warm summer temperatures in the Arctic reduce the frequency with which the statured IWV threshold is met, leading to fewer detected ARs. Consequently, this ARDT shows minimum AR-related heat, moisture transport, and minimum contributions to seasonal LWD and surface contribution climatology during summer. The distributions of AR's contributions to poleward MSE transport (Figures 2a and 2b) and IVT (Figures 3a and 3b) are similar, and both are determined by the frequency of AR occurrences (Figures 1a and 1b). However, ARs play different roles in transporting total poleward MSE and IVT, as shown in Figures S1 and S3 of Supporting Information S1. Total poleward MSE transport is largest in winter due to the strongest temperature difference between the Arctic and mid-latitudes and smallest in summer. This seasonality contrasts with total poleward IVT and detected AR occurrence frequency (except for Purdue-

85th-IVT and *polar extreme* ARDTs), which are largest in summer and are minimal in winter. Baffin Bay is the primary pathway for poleward MSE transport, but is secondary for Arctic ARs and poleward IVT. The primary pathway for poleward IVT, Arctic ARs, and the corresponding AR-IVT and AR-MSE pathways is all concentrated in the Arctic Atlantic sector. Additionally, total poleward IVT-related latent heat transport is only 1% of total poleward MSE transport. As a result, ARs, detected mainly by moisture measurement, play a larger role in transporting moisture poleward than heat, as shown by larger overall IVT contribution percentages (Figures 2 and 3) and consistency with the primary pathway of poleward IVT rather than MSE transport. In contrast to ARs, warm air intrusions, defined by temperature rather than moisture (Dekoutsidis et al., 2024), might be more reflective of poleward heat transport, particularly in the primary pathway for poleward MSE transport. This merits further investigation.

Surface LWD forcing has been recognized as an important driver of ongoing changes in sea ice extent and concentration (Huang et al., 2019; Park et al., 2015). Arctic ARs have been found to impede sea ice recovery in cold seasons by increasing LWD. This has been observed in both specific low-record sea ice years and cumulative climatological impacts studies (Hegyi & Taylor, 2017; Woods & Caballero, 2016; P. Zhang et al., 2023). Across all 12 ARDTs, ARs consistently produce significant positive surface LWD anomalies throughout the Arctic. These anomalies are most prominent in winter (increasing with latitude), followed by spring and fall, and are smallest in summer (decreasing with latitude), demonstrating strong seasonality (Figure 4a). However, their total integrated LWD during AR events constitutes only a small fraction of the seasonal climatological LWD (0.0%–15% in Figure 4b) and is strongly determined by their AR occurrence frequency (0.0%–14% in Figure 1a). Absolute threshold-based ARDTs, such as *global-specific* ARDTs, use more restrictive criteria and detect only the most extreme AR events, resulting in the largest average LWD anomalies (>100 W m^{-2}) during cold seasons and over the higher Arctic. Despite these large anomalies, their infrequent occurrence leads to a much smaller integrated contribution to seasonal climatological LWD (<1%).

In contrast, *polar-specific* ARDTs using the 85th percentile climate thresholds detect more frequent AR occurrences, producing lower average AR-LWD anomalies. Nevertheless, these more frequent AR events account for 10%–15% of seasonal LWD, leading to a substantial cumulative impact. This shows that algorithms emphasizing extreme events with large LWD anomalies do not always indicate a large overall radiative climate impact. Additionally, consistent with the AR occurrence frequency, most ARDTs (except for Purdue-85th-IVT and *polar extreme*) display the largest AR contribution to total LWD in summer and the smallest in winter, which is opposite to the seasonal pattern of AR-LWD anomalies. Compared to the AR-LWD anomalies, the seasonality of AR contribution to the total LWD is much weaker due to the smaller contribution magnitude ranges, particularly for *global-specific* and DL ARDTs. Percentile-only-based ARDTs display even smaller seasonality compared to other ARDTs yet remain consistent with their AR occurrence frequency.

Although AR-related surface precipitation anomalies may not be extreme in magnitude as AR-induced LWD anomalies, they contribute more substantially to the seasonal precipiaton climatology across all 12 ARDTs. The magnitude and spatial extent of these anomalies vary considerably by ARDT: *Global-specific* ARDTs tend to detect fewer but more intense events, resulting in high, localized precipitation anomalies with limited spatial coverage, while *polar-specific* ARDTs capture a broader spectrum of AR intensities, yielding weaker but more spatially extensive anomalies. Unlike AR-induced LWD anomalies, AR-related precipitation anomalies exhibite weaker seasonality, suggesting the thermodynamic impacts of ARs on precipitation might be less sensitive to variations in background temperature and moisture conditions. However, latitudinal variability remains pronounced, particularly in regions aligns with storm tracks and orgraphic features. Importantly, ARs contribute to seasonal precipitation totals at rates often 2 to 10 times greater than their frequency, underscoring their outsized role of ARs in surface precipitation impacts. These findings suggest that, beyond radiative forcing, surface temperature responses may also be influenced by diabatic heating associated with AR-related precipitation processes, which should be considered when evaluating Arctic surface warming in the future studies. Additionally, strong AR-related precipitation anomalies around Greenland, particularly along its eastern and western coasts, contribute significantly to surface mass balance and may accelerate ice sheet or enhance snowfall, underscoring the complex role of ARs in modulating Greenland's surface mass balance beyond their strong melting effects through changes in surface energy budgets (Mattingly et al., 2018, 2020, 2023).

Among the 12 ARDTs, Purdue-85th_IVT and *polar extreme* ARDTs are percentile-only-based algorithms. These ARDTs show minimal seasonality and smaller meridional (Figure 1a) and longitudinal gradients (Figure 1b) in

AR occurrence frequency due to their grid-point and monthly (seasonally)-dependent detection algorithms. The large longitudinal variability in total climatological MSE transport (Figures S1b and S2b in Supporting Information S1) and IVT (Figures S3b and S4b in Supporting Information S1) results in significant longitudinal variability in AR-related MSE and IVT, as well as their contributions to poleward MSE transport (Figure 2c) and IVT (Figure 3c).

Different ARDTs lead to differences in AR climatology and consequent impacts attributable to ARs in the Arctic. More restrictive climate criteria-based ARDTs, such as *global-sp*ecific and *polar extreme* ARDTs, identify extreme AR events with substantial heat and moisture (Figures 2b and 3b) and causing significant surface LWD and precipitation anomalies (Figures 4a and 5a). However, these ARDTs detect ARs less frequently thus their role in transporting total poleward heat and moisture and their impacts on climatological surface LWD forcing and precipitation are not as large (Figures 2a, 3a, 4b and 5b). *Polar-constrained* ARDTs, which use both relative and absolute thresholds, are commonly used in the Arctic (Z. Zhang et al., 2024). The use of an absolute threshold of 100 kg m^{-1} s^{-1} was initially selected to identify AR-like features and extreme precipitation events in the polar regions. This results in *polar-constrained* ARDTs identifying more extreme ARs with higher MSE and moisture transports (Figures 2b and 3b) and larger AR-LWD and surface precipitation anomalies (Figures 4a and 5a) during AR events than the non-constrained Purdue-85th-IVT ARDT. But, because they detect fewer ARs (Figure 1a) their overall contribution to seasonal MSE transport, IVT, LWD, and surface precipitation is less than for the Purdue-85th-IVT ARDT. The Purdue-85th-IVT ARDT generally shows the highest climatological contribution to MSE transport (Figure 2a), IVT (Figure 3a) and seasonal LWD forcing (Figure 4b) and precipitation contribution (Figure 5b) due to its higher AR occurrence frequency (Figure 1a) compared to other ARDTs in this study. In cold seasons, absolute-threshold ARDTs and Gorodetskaya ARDT are more effective at detecting Arctic ARs in oceanic regions, especially along the primary poleward IVT pathway in the Arctic Atlantic sector. Conversely, percentile-only ARDTs tend to identify more ARs over continental areas and have less spatial variability than absolute-threshold ARDTs.

In summary, this study presents the first comprehensive evaluation of 12 widely used ARDTs in the Arctic, revealing substantial variability in their ability to detect ARs and quantify their impacts on atmospheric heat and moisture transport, surface radiative forcing, and precipitation. Crucially, we show that the choice of ARDT directly influences estimates of Arctic energy and moisture budgets, particularly MSE transport and IVT, which in turn affect surface radiative and energy budgets, and hydrological extremes. These differences have critical implications for interpreting AR-driven process under Arctic amplification, with direct relevance to sea ice loss, glacier melt, warming extremes, and broader Arctic hydrological changes.

Our results demonstrate that global ARDTs, while widely used in the midlatitude studies to capture extreme precipitation events, severely underestimate AR frequency and their cumulative impacts in the Arctic due to the restrictive thresholds that are not appropriate for its dry and cold Arctic environment. Their use in the polar contexts can therefore yield misleading conclusions, especially when assessing climatological impact. These *global-specific* ARDTs emphasize rare, extreme AR events associated with large LWD anomalies, while overlooking the more frequent yet less intense ARs that nonetheless transport substantial moisture and energy poleward, driving significant changes in Arctic's radiative and energy budgets. As a result, they fail to capture the full extent of AR-driven surface warming and sea ice decline, leading to a systematic underestimation of AR's role in Arctic amplification. Similarly, although these ARDTs may attribute up to 10 times more precipitation than expected from their low AR frequency, such extreme events are rare, often occurring only once per season in 20 years, or not at all.

We therefore recommend that future Arctic AR research avoid relying on global ARDTs and instead prioritize the use of *polar-specific* ARDTs, which are better suited to capturing the frequency, spatial distribution, and climatological significance of ARs in this unique environment. Because large-scale climate variability strongly modulates the spatial and temporal clustering of AR occurrences (C. Zhang et al., 2023; Zhou et al., 2024), *polar-specific* ARDTs are more effective at identifying consecutive, back-to-back ARs that affect the Arctic over short time intervals. Accurately representing these clustered events is essential for improving subseasonal-to-seasonal (S2S) prediction of Arctic ARs (DeFlorio et al., 2024; Yang et al., 2024). Furthermore, *polar-specific* ARDTs can more accurately assess the contributions of ARs to Arctic climate change, including surface and snowpack warming, earlier sea ice melt onset in spring, delayed refreeze in fall and winter, and their broader role of ARs in accelerating Arctic amplification. Within the category of polar-specific ARDTs, the choice of specific method

should be adaptive to the specific types of impact being investigated, the region of interest (e.g., continents vs. oceans), and timing (e.g., seasonal variation). This study advances the understanding of Arctic ARs, their effects on the climate system, and the variability in the results based on the selected ARDT. It provides valuable insights for the future application of ARDTs in Arctic research. Climate change poses another important consideration for appropriate application of ARDTs. As atmospheric temperature and moisture increase following the Clausius-Clapeyron equation, the absolute threshold-based ARDTs may become less effective in detecting ARs under climate change scenarios due to fixed thresholds that do not account for a rising moisture field. Meanwhile, percentile threshold-based ARDTs, which adapt to both the current climate conditions and future projections, warrant further investigation to fully understand AR behavior and impacts in a rapidly changing climate.

Conflict of Interest

The authors declare no conflicts of interest relevant to this study.

Acknowledgments

Zhang is supported by the Cooperative Institute for Research in Environmental Sciences (CIRES) Visiting Fellows Program, funded by the National Oceanic and Atmospheric Administration (NOAA) Cooperative Agreement NA22OAR4320151. Cassano and Seefeldt, are supported by the Regional and Global Model Analysis (RGMA) component of the Earth and Environmental System Modeling (EESM) program of the U.S. Department of Energy's Office of Science, as a contribution to the HiLAT-RASM project (contract no. DE-SC0024872). Tung was partially support by NSF OAC-2232872. Tung was supported while serving at the National Science Foundation; the findings and conclusions expressed herein do not necessarily reflect the views of the NSF or the U.S. Government. Collins and Mahesh are supported by the Office of Science, Office of Biological and Environmental Research of the U.S. Department of Energy, as part of the Regional and Global Model Analysis program area, within the Earth and Environmental Systems Modeling Program (contract no. DE-AC02-05CH11231) via the CASCADE Scientific Focus Area at LBNL. We are extremely grateful for the helpful discussions with Dr. Aaron Donohoe and Dr. Tyler Cox, particularly Dr. Tyler Cox for generously sharing his code for computing the mass-corrected atmospheric heat transport. We extend our deepest gratitude to the ARDT developers for their valuable contributions to this intercomparison study: Dr. Kyle Mattingly (Mattingly ARDT), Dr. Weiming Ma (M24 ARDT), Dr. Irina Gorodetskaya and Dr. Melanie Lauer (Gorodetskaya ARDT), and Dr. Jonathan Wille (Wille-vIVT and Wille-IWV ARDTs). We also acknowledge Purdue Information Technology at Purdue (ITAP) Rosen Center for Advanced Computing (RCAC) for their generous assistance with data-intensive high-performance computing. Additionally, we thank Dr. Qinqin Kong for facilitating access to the ERA5 data, as well as two anonymous reviewers for their insightful comments to improve the manuscript.

Data Availability Statement

ERA5 data (Hersbach et al., 2020) were acquired from the Copernicus Climate Change Service (C3S) Climate Data Store (https://cds.climate.copernicus.eu/cdsapp#!/dataset/reanalysis-era5-single-levels?tab=form). The Purdue-85th-IVT ARDT is openly accessible at https://purr.purdue.edu/publications/4322/1 (Tung et al., 2023). M24 ARDT, Mattingly ARDT, Gorodetskaya ARDT and Wille-vIVT and Wille-IWV ARDTs were provided directly by their respective developers and are available upon request from the corresponding author, Chen Zhang (chen.zhang-3@colorado.edu). Other ARDTs, including Guan-Waliser, Mundhenk_v3, Lora_v2, AR-Connect, TempestLR, and ClimateNet, can be accessed through the NSF NCAR Research Data Archive (RDA) (Collow et al., 2022a). All computational code required to replicate the presented results in this study is available upon request from the corresponding author, Chen Zhang (chen.zhang-3@colorado.edu).

References

Baggett, C., Lee, S., & Feldstein, S. (2016). An investigation of the presence of atmospheric rivers over the North Pacific during planetary-scale wave life cycles and their role in Arctic warming. *Journal of the Atmospheric Sciences*, *73*(11), 4329–4347. https://doi.org/10.1175/JAS-D-16-0033.1

Chen, X., Leung, L. R., Gao, Y., Liu, Y., Wigmosta, M., & Richmond, M. (2018). Predictability of extreme precipitation in Western U.S. watersheds based on atmospheric river occurrence, intensity, and duration. *Geophysical Research Letters*, *45*(21). https://doi.org/10.1029/2018GL079831

Chen, Y., Aires, F., Francis, J. A., & Miller, J. R. (2006). Observed relationships between Arctic longwave cloud forcing and cloud parameters using a neural network. *Journal of Climate*, *19*(16), 4087–4104. https://doi.org/10.1175/JCLI3839.1

Clark, J. P., Feldstein, S. B., & Lee, S. (2022). Moist static energy transport trends in four global reanalyses: Are they downgradient? *Geophysical Research Letters*, *49*(20), e2022GL098822. https://doi.org/10.1029/2022GL098822

Cohen, J., Screen, J. A., Furtado, J. C., Barlow, M., Whittleston, D., Coumou, D., et al. (2014). Recent Arctic amplification and extreme mid-latitude weather. *Nature Geoscience*, *7*(9), 627–637. https://doi.org/10.1038/ngeo2234

Collow, A. B. M., Shields, C. A., Guan, B., Kim, S., Lora, J. M., McClenny, E. E., et al. (2022a). Atmospheric River tracking method intercomparison project tier 2 reanalysis source data and catalogues [Dataset]. *NSF National Center for Atmospheric Research*. https://doi.org/10.26024/rawv-yx53

Collow, A. B. M., Shields, C. A., Guan, B., Kim, S., Lora, J. M., McClenny, E. E., et al. (2022b). An overview of ARTMIP's tier 2 reanalysis intercomparison: Uncertainty in the detection of atmospheric Rivers and their associated precipitation. *Journal of Geophysical Research: Atmospheres*, *127*(8), e2021JD036155. https://doi.org/10.1029/2021JD036155

Cox, T., Donohoe, A., Armour, K. C., Frierson, D. M., & Roe, G. H. (2023). Comment on "Moist static energy transport trends in four global reanalyses: Are they downgradient?" by Clark et al. (2022). *Geophysical Research Letters*, *50*(15), e2023GL102804. https://doi.org/10.1029/2023gl102804

Cox, T., Donohoe, A., Armour, K. C., Roe, G. H., & Frierson, D. M. (2024). A new method for calculating instantaneous atmospheric heat transport. *Journal of Climate*, *37*(17), 4337–4346. https://doi.org/10.1175/jcli-d-23-0521.1

DeFlorio, M. J., Sengupta, A., Castellano, C. M., Wang, J., Zhang, Z., Gershunov, A., et al. (2024). From California's extreme drought to major flooding: Evaluating and synthesizing experimental seasonal and subseasonal forecasts of landfalling atmospheric rivers and extreme precipitation during winter 2022/23. *Bulletin of the American Meteorological Society*, *105*(1), E84–E104. https://doi.org/10.1175/bams-d-22-0208.1

Dekoutsidis, G., Wirth, M., & Groß, S. (2024). The effects of warm-air intrusions in the high Arctic on cirrus clouds. *Atmospheric Chemistry and Physics*, *24*(10), 5971–5987. https://doi.org/10.5194/acp-24-5971-2024

Dufour, A., Zolina, O., & Gulev, S. K. (2016). Atmospheric moisture transport to the arctic: Assessment of reanalyses and analysis of transport components. *Journal of Climate*, *29*(14), 5061–5081. https://doi.org/10.1175/JCLI-D-15-0559.1

Gelaro, R., McCarty, W., Suárez, M. J., Todling, R., Molod, A., Takacs, L., et al. (2017). The modern-era retrospective analysis for research and applications, version 2 (MERRA-2). *Journal of Climate*, *30*(14). https://doi.org/10.1175/JCLI-D-16-0758.1

Gorodetskaya, I. V., Silva, T., Schmithuesen, H., & Hirasawa, N. (2020). Atmospheric river signatures in radiosonde profiles and re- analyses at the Dronning Maud Land Coast, East Antarctica. *Advances in Atmospheric Sciences*, *37*(5), 455–476. https://doi.org/10.1007/s00376-020-9221-8

Gorodetskaya, I. V., Tsukernik, M., Claes, K., Ralph, M. F., Neff, W. D., & Van Lipzig, N. P. M. (2014). The role of atmospheric rivers in anomalous snow accumulation in East Antarctica. *Geophysical Research Letters*, *41*(17), 6199–6206. https://doi.org/10.1002/2014GL060881

Graham, R. M., Hudson, S. R., & Maturilli, M. (2019). Improved performance of ERA5 in Arctic gateway relative to four global atmospheric reanalyses. *Geophysical Research Letters*, *46*(11), 6138–6147. https://doi.org/10.1029/2019GL082781
Graversen, R. G., & Burtu, M. (2016). Arctic amplification enhanced by latent energy transport of atmospheric planetary waves. *Quarterly Journal of the Royal Meteorological Society*, *142*(698), 2046–2054. https://doi.org/10.1002/qj.2802
Graversen, R. G., Mauritsen, T., Tjernström, M., Källén, E., & Svensson, G. (2008). Vertical structure of recent Arctic warming. *Nature*, *451*(7174). https://doi.org/10.1038/nature06502
Guan, B., & Waliser, D. E. (2015). Detection of atmospheric rivers: Evaluation and application of an algorithm for global studies. *Journal of Geophysical Research*, *120*(24), 12514–12535. https://doi.org/10.1002/2015JD024257
Guan, B., & Waliser, D. E. (2019). Tracking atmospheric rivers globally: Spatial distributions and temporal evolution of life cycle characteristics. *Journal of Geophysical Research*, *124*(23), 12523–12552. https://doi.org/10.1029/2019JD031205
Hegyi, B. M., & Taylor, P. C. (2017). The regional influence of the Arctic oscillation and Arctic Dipole on the wintertime Arctic surface radiation budget and sea ice growth. *Geophysical Research Letters*, *44*(9), 4341–4350. https://doi.org/10.1002/2017GL073281
Hegyi, B. M., & Taylor, P. C. (2018). The unprecedented 2016–2017 Arctic sea ice growth season: The crucial role of atmospheric rivers and longwave fluxes. *Geophysical Research Letters*, *45*(10), 5204–5212. https://doi.org/10.1029/2017gl076717
Hersbach, H., Bell, B., Berrisford, P., Hirahara, S., Horányi, A., Muñoz-Sabater, J., et al. (2020). The ERA5 global reanalysis. *Quarterly Journal of the Royal Meteorological Society*, *146*(730), 1999–2049. https://doi.org/10.1002/qj.3803
Huang, Y., Dong, X., Bailey, D. A., Holland, M. M., Xi, B., DuVivier, A. K., et al. (2019). Thicker clouds and accelerated Arctic Sea ice decline: The atmosphere-sea ice interactions in spring. *Geophysical Research Letters*, *46*(12), 6980–6989. https://doi.org/10.1029/2019GL082791
Lauer, M., Rinke, A., Gorodetskaya, I., Sprenger, M., Mech, M., & Crewell, S. (2023). Influence of atmospheric rivers and associated weather systems on precipitation in the Arctic. *Atmospheric Chemistry and Physics*, *23*(15), 8705–8726. https://doi.org/10.5194/acp-23-8705-2023
Lavers, D. A., & Villarini, G. (2013). Atmospheric rivers and flooding over the central United States. *Journal of Climate*, *26*(20), 7829–7836. https://doi.org/10.1175/JCLI-D-13-00212.1
Lavers, D. A., & Villarini, G. (2015). The contribution of atmospheric rivers to precipitation in Europe and the United States. *Journal of Hydrology*, *522*, 382–390. https://doi.org/10.1016/j.jhydrol.2014.12.010
Lavers, D. A., Villarini, G., Allan, R. P., Wood, E. F., & Wade, A. J. (2012). The detection of atmospheric rivers in atmospheric reanalyses and their links to British winter floods and the large-scale climatic circulation. *Journal of Geophysical Research*, *117*(20). https://doi.org/10.1029/2012JD018027
Leung, L. R., & Qian, Y. (2009). Atmospheric rivers induced heavy precipitation and flooding in the western U.S. simulated by the WRF regional climate model. *Geophysical Research Letters*, *36*(3). https://doi.org/10.1029/2008GL036445
Liu, C., & Barnes, E. A. (2015). Extreme moisture transport into the Arctic linked to Rossby wave breaking. *Journal of Geophysical Research: Atmospheres*, *120*(9), 3774–3788. https://doi.org/10.1002/2014JD022796
Luo, Q., & Tung, W. W. (2015). Case study of moisture and heat budgets within atmospheric rivers. *Monthly Weather Review*, *143*(10), 4145–4162. https://doi.org/10.1175/MWR-D-15-0006.1
Ma, W., Chen, G., Peings, Y., & Alviz, N. (2021). Atmospheric River response to Arctic Sea ice loss in the polar amplification model intercomparison project. *Geophysical Research Letters*, *48*(20), e2021GL094883. https://doi.org/10.1029/2021GL094883
Ma, W., Wang, H., Chen, G., Leung, L. R., Lu, J., Rasch, P. J., et al. (2024). The role of interdecadal climate oscillations in driving Arctic atmospheric river trends. *Nature Communications*, *15*(1), 2135. https://doi.org/10.1038/s41467-024-45159-5
Maclennan, M. L., Lenaerts, J. T. M., Shields, C. A., Hoffman, A. O., Wever, N., Thompson-Munson, M., et al. (2023). Climatology and surface impacts of atmospheric rivers on West Antarctica. *The Cryosphere*, *17*(2), 865–881. https://doi.org/10.5194/tc-17-865-2023
Mahesh, A., Collins, W. D., Boos, W. R., Obrien, T. A., & Zhou, Y. (2025). Constraining atmospheric river uncertainty using instantaneous poleward latent heat transport. *arXiv*. preprint arXiv:2509.12807. https://doi.org/10.48550/arXiv.2509.12807
Mattingly, K. S., Mote, T. L., & Fettweis, X. (2018). Atmospheric river impacts on Greenland ice sheet surface mass balance. *Journal of Geophysical Research: Atmospheres*, *123*(16), 8538–8560. https://doi.org/10.1029/2018JD028714
Mattingly, K. S., Mote, T. L., Fettweis, X., As, D. V., Tricht, K. V., Lhermitte, S., et al. (2020). Strong summer atmospheric rivers trigger Greenland ice sheet melt through spatially varying surface energy balance and cloud regimes. *Journal of Climate*, *33*(16), 6809–6832. https://doi.org/10.1175/JCLI-D-19-0835.1
Mattingly, K. S., Turton, J. V., Wille, J. D., Noël, B., Fettweis, X., Rennermalm, Å. K., & Mote, T. L. (2023). Increasing extreme melt in northeast Greenland linked to Foehn winds and atmospheric rivers. *Nature Communications*, *14*(1), 1743. https://doi.org/10.1038/s41467-023-37434-8
McClenny, E. E., Ullrich, P. A., & Grotjahn, R. (2020). Sensitivity of atmospheric river vapor transport and precipitation to uniform sea surface temperature increases. *Journal of Geophysical Research: Atmospheres*, *125*(21), e2020JD033421. https://doi.org/10.1029/2020JD033421
Mortin, J., Svensson, G., Graversen, R. G., Kapsch, M. L., Stroeve, J. C., & Boisvert, L. N. (2016). Melt onset over Arctic sea ice controlled by atmospheric moisture transport. *Geophysical Research Letters*, *43*(12), 6636–6642. https://doi.org/10.1002/2016GL069330
Mundhenk, B. D., Barnes, E. A., & Maloney, E. D. (2016). All-season climatology and variability of atmospheric river frequencies over the North Pacific. *Journal of Climate*, *29*(13), 4885–4903. https://doi.org/10.1175/JCLI-D-15-0655.1
Nash, D., Waliser, D., Guan, B., Ye, H., & Ralph, F. M. (2018). The role of atmospheric Rivers in extratropical and polar hydroclimate. *Journal of Geophysical Research: Atmospheres*, *123*(13), 6804–6821. https://doi.org/10.1029/2017JD028130
Neff, W. (2018). Atmospheric rivers melt Greenland. *Nature Climate Change*, *8*(10), 857–858. https://doi.org/10.1038/s41558-018-0297-4
Neiman, P. J., Ralph, F. M., Wick, G. A., Lundquist, J. D., & Dettinger, M. D. (2008). Meteorological characteristics and overland precipitation impacts of atmospheric rivers affecting the West coast of North America based on eight years of SSM/I satellite observations. *Journal of Hydrometeorology*, *9*(1), 22–47. https://doi.org/10.1175/2007JHM855.1
O'Brien, T. A., Payne, A. E., Shields, C. A., Rutz, J., Brands, S., Castellano, C., et al. (2020). Detection uncertainty matters for understanding atmospheric rivers. *Bulletin of the American Meteorological Society*, *101*. https://doi.org/10.1175/BAMS-D-19-0348.1
O'Brien, T. A., Wehner, M. F., Payne, A. E., Shields, C. A., Rutz, J. J., Leung, L. R., et al. (2022). Increases in future AR count and size: Overview of the ARTMIP tier 2 CMIP5/6 experiment. *Journal of Geophysical Research: Atmospheres*, *127*(6). https://doi.org/10.1029/2021JD036013
Park, D.-S. R., Lee, S., & Feldstein, S. B. (2015). Attribution of the recent winter Sea ice decline over the Atlantic sector of the Arctic Ocean. *Journal of Climate*, *28*(10), 4027–4033. https://doi.org/10.1175/jcli-d-15-0042.1
Prabhat, Kashinath, K., Mudigonda, M., Kim, S., Kapp-Schwoerer, L., Graubner, A., et al. (2021). ClimateNet: An expert-labeled open dataset and deep learning architecture for enabling high-precision analyses of extreme weather. *Geoscientific Model Development*, *14*(1), 107–124. https://doi.org/10.5194/gmd-14-107-2021
Ralph, F. M., Dettinger, M., Lavers, D., Gorodetskaya, I. V., Martin, A., Viale, M., et al. (2017). Atmospheric rivers emerge as a global science and applications focus. *Bulletin of the American Meteorological Society*, *98*(9), 1969–1973. https://doi.org/10.1175/BAMS-D-16-0262.1

Ralph, F. M., Dettinger, M. C. L. D., Cairns, M. M., Galarneau, T. J., & Eylander, J. (2018). Defining "Atmospheric River": How the glossary of meteorology helped resolve a debate. *Bulletin of the American Meteorological Society*, *99*(4), 837–839. https://doi.org/10.1175/BAMS-D-17-0157.1

Ralph, F. M., Neiman, P. J., & Wick, G. A. (2004). Satellite and CALJET aircraft observations of atmospheric rivers over the Eastern North Pacific Ocean during the winter of 1997/98. *Monthly Weather Review*, *132*(7), 1721–1745. https://doi.org/10.1175/1520-0493(2004)132<1721:SACAOO>2.0.CO;2

Ralph, F. M., Neiman, P. J., Wick, G. A., Gutman, S. I., Dettinger, M. D., Cayan, D. R., & White, A. B. (2006). Flooding on California's Russian River: Role of atmospheric rivers. *Geophysical Research Letters*, *33*(13). https://doi.org/10.1029/2006GL026689

Rutz, J. J., James Steenburgh, W., & Martin Ralph, F. (2014). Climatological characteristics of atmospheric rivers and their inland penetration over the Western United States. *Monthly Weather Review*, *142*(2), 905–921. https://doi.org/10.1175/MWR-D-13-00168.1

Rutz, J. J., Shields, C. A., Lora, J. M., Payne, A. E., Guan, B., Ullrich, P., et al. (2019). The atmospheric river tracking method intercomparison project (ARTMIP): Quantifying uncertainties in atmospheric river climatology. *Journal of Geophysical Research: Atmospheres*, *124*(24), 13777–13802. https://doi.org/10.1029/2019JD030936

Serreze, M. C., Barrett, A. P., Slater, A. G., Steele, M., Zhang, J., & Trenberth, K. E. (2007). The large-scale energy budget of the Arctic. *Journal of Geophysical Research*, *112*(D11). https://doi.org/10.1029/2006jd008230

Serreze, M. C., Barrett, A. P., Stroeve, J. C., Kindig, D. N., & Holland, M. M. (2009). The emergence of surface-based Arctic amplification. *The Cryosphere*, *3*(1), 11–19. https://doi.org/10.5194/tc-3-11-2009

Serreze, M. C., & Barry, R. G. (2011). Processes and impacts of Arctic amplification: A research synthesis. *Global and Planetary Change*, *77*(1–2), 85–96. https://doi.org/10.1016/j.gloplacha.2011.03.004

Shearer, E. J., Nguyen, P., Sellars, S. L., Analui, B., Kawzenuk, B., Hsu, K. L., & Sorooshian, S. (2020). Examination of global midlatitude atmospheric river lifecycles using an object-oriented methodology. *Journal of Geophysical Research: Atmospheres*, *125*(22), e2020JD033425. https://doi.org/10.1029/2020JD033425

Shields, C. A., Rutz, J. J., Leung, L. Y., Martin Ralph, F., Wehner, M., Kawzenuk, B., et al. (2018). Atmospheric river tracking method intercomparison project (ARTMIP): Project goals and experimental design. *Geoscientific Model Development*, *11*(6), 2455–2474. https://doi.org/10.5194/gmd-11-2455-2018

Shields, C. A., Wille, J. D., Marquardt Collow, A. B., Maclennan, M., & Gorodetskaya, I. V. (2022). Evaluating uncertainty and modes of variability for Antarctic atmospheric Rivers. *Geophysical Research Letters*, *49*(16), e2022GL099577. https://doi.org/10.1029/2022GL099577

Skinner, C. B., Lora, J. M., Payne, A. E., & Poulsen, C. J. (2020). Atmospheric river changes shaped mid-latitude hydroclimate since the mid-Holocene. *Earth and Planetary Science Letters*, *541*, 116293. https://doi.org/10.1016/j.epsl.2020.116293

Taylor, P. C., Boeke, R. C., Boisvert, L. N., Feldl, N., Henry, M., Huang, Y., et al. (2022). Process drivers, inter-model spread, and the path forward: A review of amplified arctic warming. *Frontiers in Earth Science*, *9*, 758361. https://doi.org/10.3389/feart.2021.758361

Tilinina, N., Gulev, S. K., Rudeva, I., & Koltermann, P. (2013). Comparing cyclone life cycle characteristics and their interannual variability in different reanalyses. *Journal of Climate*, *26*(17), 6419–6438. https://doi.org/10.1175/JCLI-D-12-00777.1

Tung, W., Zhang, C., & Cleveland, W. S. (2023). *Arctic atmospheric river Labels and climatology based on 3-hourly ERA5 and MERRA-2 from 1980 to 2019*. Purdue University Research Repository.

Wille, J. D., Favier, V., Dufour, A., Gorodetskaya, I. V., Turner, J., Agosta, C., & Codron, F. (2019). West Antarctic surface melt triggered by atmospheric rivers. *Nature Geoscience*, *12*(11), 911–916. https://doi.org/10.1038/s41561-019-0460-1

Wille, J. D., Favier, V., Gorodetskaya, I. V., Agosta, C., Kittel, C., Beeman, J. C., et al. (2021). Antarctic atmospheric River climatology and precipitation impacts. *Journal of Geophysical Research: Atmospheres*, *126*(8), e2020JD033788. https://doi.org/10.1029/2020JD033788

Woods, C., & Caballero, R. (2016). The role of moist intrusions in winter Arctic warming and sea ice decline. *Journal of Climate*, *29*(12), 4473–4485. https://doi.org/10.1175/jcli-d-15-0773.1

Woods, C., Caballero, R., & Svensson, G. (2013). Large-scale circulation associated with moisture intrusions into the Arctic during winter. *Geophysical Research Letters*, *40*(17), 4717–4721. https://doi.org/10.1002/grl.50912

Yang, Z., DeFlorio, M. J., Sengupta, A., Wang, J., Castellano, C. M., Gershunov, A., et al. (2024). Seasonality and climate modes influence the temporal clustering of unique atmospheric rivers in the Western US. *Communications Earth & Environment*, *5*(1), 734. https://doi.org/10.1038/s43247-024-01890-x

Zhang, C., Cassano, J. J., Seefeldt, M., Wang, H., Ma, W., & Tung, W. (2025). Quantifying the impacts of Atmos Pheric Rivers on the surface energy budget of the Arctic based on reanalysis. *The Cryosphere*, *19*(10), 4671–4699. https://doi.org/10.5194/tc-19-4671-2025

Zhang, C., Tung, W., & Cleveland, W. S. (2023). Climatology and decadal changes of Arctic atmospheric Rivers based on ERA5 and MERRA-2. *Environmental Research: Climate*. https://doi.org/10.1088/2752-5295/adf0f

Zhang, C., Tung, W. W., & Cleveland, W. S. (2021). In search of the optimal Atmospheric river index for US precipitation: A multifactorial analysis. *Journal of Geophysical Research: Atmospheres*, *126*(10), e2020JD033667. https://doi.org/10.1029/2020JD033667

Zhang, P., Chen, G., Ting, M., Ruby Leung, L., Guan, B., & Li, L. (2023). More frequent atmospheric rivers slow the seasonal recovery of Arctic sea ice. *Nature Climate Change*, *13*(3), 266–273. https://doi.org/10.1038/s41558-023-01599-3

Zhang, R., Wang, H., Fu, Q., Rasch, P. J., Wu, M., & Maslowski, W. (2021). Understanding the cold season arctic surface warming trend in recent decades. *Geophysical Research Letters*, *48*(19), e2021GL094878. https://doi.org/10.1029/2021GL094878

Zhang, Z., Ralph, F. M., Zou, X., Kawzenuk, B., Zheng, M., Gorodetskaya, I. V., et al. (2024). Extending the center for Western weather and water extremes (CW3E) atmospheric river scale to the polar regions. *The Cryosphere*, *18*(11), 5239–5258. https://doi.org/10.5194/tc-18-5239-2024

Zhou, Y., Wehner, M., & Collins, W. (2024). Back-to-back high category atmospheric river landfalls occur more often on the west coast of the United States. *Communications Earth & Environment*, *5*(1), 187. https://doi.org/10.1038/s43247-024-01368-w

Zhu, Y., & Newell, R. E. (1998). A proposed algorithm for moisture fluxes from atmospheric rivers. *Monthly Weather Review*, *126*(3), 725–735. https://doi.org/10.1175/1520-0493(1998)126<0725:APAFMF>2.0.CO;2